# MODELING OF STRATIFORM CLOUDINESS AND PRECIPITATION IN MESOSCALE AND LARGE SCALE MODELS

Peter Bechtold and Jean-Pierre Pinty
Laboratoire d'Aerologie, Université Paul Sabatier
Toulouse, France

## Introduction

The main point of this seminar will be the representation of cloudiness in the planetary boundary-layer, given the fact that cloudiness plays an important role in accurate local and global climate modeling. The aim is to develop a parameterization of the cloud-topped boundary layer (CTBL) which i) includes in a consistent way a turbulent scheme based on the turbulent kinetic energy, a statistical description of subgrid cloudiness, and a microphysical scheme, and ii) is sufficiently simple and accurate in order to be implemented in mesoscale and large-scale models.

In the first part we discuss some details of the order 1.5 turbulence scheme and its coupling with a statistical partial cloudiness scheme. A 1D version of a 3D hydrostatic mesoscale model is used to show the performance of the scheme for selected cases of boundary layer cloudiness, and to discuss some numerical consequences (vertical resolution, model stability) adherent to the use of a statistical partial cloudiness scheme. The second part focuses on the modeling of subgrid-scale precipitation including the description of microphysical processes in partly cloudy layers. A general method is presented of how to include the effects of partial cloudiness in a bulk microphysical scheme and so to account for both subgrid-scale stratiform precipitation and subgrid-scale convective precipitation.

### 1.1. Model description

After a brief description of the basic model equations we will focus on some particularities of the turbulence and condensation (partial condensation) schemes which are specific to the problem of modeling the cloud-topped boundary layer at the large and mesoscale. A more detailed discussion of these schemes and their implementation in a 3D hydrostatic mesoscale model are given in Bechtold et al. (1992a,b) (hereafter B92).

In 1D the basic prognostic model equations for the horizontal wind components and the quasi-conservative thermodynamic variables liquid potential temperature and total water content write:

$$\frac{\partial u}{\partial t} = -w\frac{\partial u}{\partial z} + f(v - v_g) - \frac{\partial}{\partial z}\overline{w'u'} \tag{1.1}$$

$$\frac{\partial v}{\partial t} = -w\frac{\partial v}{\partial z} - f(u - u_g) - \frac{\partial}{\partial z}\overline{w'v'} \tag{1.2}$$

$$\frac{\partial \theta_l}{\partial t} = -w\frac{\partial \theta_l}{\partial z} + \frac{\partial \theta_l}{\partial t}|_{rad} - \frac{\partial}{\partial z}\overline{w'\theta_l'} - \frac{Lq_l}{C_pT}\frac{\partial q_w}{\partial t}|_{rain} \tag{1.3}$$

$$\frac{\partial q_w}{\partial t} = -w\frac{\partial q_w}{\partial z} + \frac{\partial q_w}{\partial t}|_{rain} - \frac{\partial}{\partial z}\overline{w'q_w'} \tag{1.4}$$

The notations are classical, and a list of symbols is provided in the Appendix. The radiative forcing term appearing in (1.3) includes both longwave and shortwave radiative processes. For simplicity, the drizzle term $\frac{\partial q_w}{\partial t}|_{rain}$ (a sink for $q_w$, and a heat source for $\theta_l$) is ignored in this part. This term will be extensively discussed in the next part devoted to subgrid precipitation.

*a) TURBULENCE SCHEME*

The turbulent fluxes $\overline{w'\chi'}$, where $\chi$ is any of the prognostic variables in Eqs. (1.1) to (1.4), are calculated with the classical K-closure mixing coefficient :

$$\overline{w'\chi'} = -K\frac{\partial \chi}{\partial z} \tag{1.5}$$

$$K = c_K\, l_K\, e^{1/2}. \tag{1.6}$$

In (1.6), $l_K$ is a characteristic mixing length and $e$ is the turbulent kinetic energy, calculated by the prognostic equation

$$\frac{\partial e}{\partial t} = -w\frac{\partial e}{\partial z} - g\frac{\overline{w'\rho'}}{\rho_0} - \overline{w'u'}\frac{\partial u}{\partial z} - \overline{w'v'}\frac{\partial v}{\partial z} - \frac{\partial}{\partial z}(\overline{w'e} - \frac{\overline{w'p'}}{\rho}) - c_\epsilon\frac{e^{3/2}}{l_\epsilon}, \tag{1.7}$$

where $l_\epsilon$ is the dissipation length. The numerical constants $c_K$ and $c_\epsilon$ have been calibrated by Bougeault and Lacarrère (1989) in the context of a convective boundary layer, we retain their values ($c_K = 0.4$, $c_\epsilon = 0.714$) to preserve the generality of the approach. All the turbulent fluxes are expressed according to (1.7). However, the buoyancy flux term $\overline{w'\rho'}/\rho_0$ necessitates a separate discussion.

*1) Formulation of the buoyancy flux*

In the presence of liquid water, the buoyancy flux term in (1.7) writes as:

$$\frac{\overline{w'\rho'}}{\rho_0} = -\frac{\overline{w'\theta'_{vl}}}{\theta_0}, \tag{1.8}$$

where $\theta_{vl} = \theta\,(1+0.61\,q_w - 1.61\,q_l)$ is the virtual potential temperature. Following Deardorff (1976), the buoyancy flux must be expressed in terms of conservative prognostic variables which are $\theta_l$ and $q_w$. We therefore have:

- clear sky case:

$$\overline{w'\theta'_{vl}}|_{clear} = (1 + 0.61\,q_w)\ \overline{w'\theta'_l} + 0.61\,\theta_0\ \overline{w'q'_w} \tag{1.9a}$$

- fully saturated case:

$$\overline{w'\theta'_{vl}}|_{sat} = \left[(1 + 0.61\,q_w) - E\left(\frac{L}{c_pT}(1 + 0.61\,q_w) - 1.61\right)\right]\ \overline{w'\theta'_l} + \left[\frac{L}{c_pT} - 1\right]\theta_0\ \overline{w'q'_w} \tag{1.9b}$$

with $E = 0.622\frac{L}{RT}q_s/(1 + 0.622\frac{L}{RT}\frac{L}{c_pT}q_s)$.

For partly saturated layers, a simple linear interpolation between the fully saturated case and subsaturated case has been chosen:

$$\overline{w'\theta'_{vl}} = N\ \overline{w'\theta'_{vl}}|_{sat} + (1-N)\ \overline{w'\theta'_{vl}}|_{clear}. \tag{1.9c}$$

In (1.9c), $N$ stands for the partial cloudiness or more correctly, the mean grid volume fraction occupied by the cloud. It can be shown that the linear interpolation in (1.9c) is valid for a CTBL, where the vertical veolcity follows a gaussian distribution.

*2) Turbulence closure*

The derivation of the internal length scales of turbulence follows the original "upward/downward free path" concept originally introduced by Bougeault and André (1986). The subsequent mixing and dissipation lengths, needed for a K-closure turbulence scheme, have been already used by Bougeault and Lacarrère (1989) in a dry mesoscale model. Briefly, the mixing length ($l_K$) and the dissipation length ($l_\epsilon$) issue from averaging two natural length scales $l_{up}$ and $l_{down}$. The length $l_{up}$ ($l_{down}$) equals the distance between an initial level of an upward (downward) moving particle and the level at which its final buoyant energy becomes zero. The fueling energy is the initial local TKE of the particle. So one has,

$$\int_z^{z+l_{up}} \frac{g}{\theta_0}(\theta_{vl}(z') - \theta_{vl}(z))\ dz' = e(z) \tag{1.10a}$$

$$\int_{z-l_{down}}^{z} \frac{g}{\theta_0}(\theta_{vl}(z) - \theta_{vl}(z'))\ dz' = e(z). \tag{1.10b}$$

Clearly, in the case of well-mixed capped boundary layers, $l_{up}$ is bounded by the inversion level and $l_{down}$ by the distance to the earth surface. For either of the two length scales $l_\epsilon$ and $l_K$ an average operator has been chosen which prefers the smaller of the two length scales $l_{up}$ and $l_{down}$. Here we have chosen:

$$l_K = Min(l_{up}, l_{down}) \tag{1.11a}$$

$$\frac{1}{l_\epsilon} = \frac{1}{2}\left(\frac{1}{l_{up}} + \frac{1}{l_{down}}\right) F(Ri) \tag{1.11b}$$

$$F(Ri) = \begin{cases} \frac{4}{3}, & Ri \le 0 \\ 1 + \frac{1}{3+Ri}, & Ri > 0 \end{cases}$$

The definition of $l_K$ in (1.11a) follows Bougeault and Lacarrère (1989). When the factor $F(Ri)$ is omitted in (1.11b), the definition of $l_\epsilon$ corresponds to that used in Bougeault and André (1986). The additional factor $F(Ri)$, where $Ri$ is the local Richardson number, has been added in (1.11b) in order to take into account the effects of wind shear. This correction factor increases the dissipation rate and so limits the TKE in cases with strong

vertical wind shear. With the chosen expression (1.11b) for the dissipation length we approach in the stable case to the formulation used by Deardorff (1980). As noted by Deardorff (1980), the turbulent length scales should be limited to some minimum value, $l_{min}$, which is less than the vertical grid spacing, $\Delta z$. This is particularly important when $l_{up}$ and $l_{down}$ are computed at levels close to regions where a stability transition occurs. We retain $l_{min} = 10$ m since the vertical resolution is set to 50 m.

*b) PARTIAL CLOUDINESS SCHEME*

A statistical description of subgrid scale condensation processes was first suggested by Sommeria and Deardorff (1977). The basic idea of their scheme is to suppose that the turbulent fluctuations of the $\theta_l$ and $q_w$ variables possess a joint normal probability distribution. Unfortunately, the original sheme necessitates the evaluation of a double integral. Mellor (1977) showed that the problem can be reduced to an integration over one variable by introducing an intermediate variable $s = a/2\ (q'_w - \alpha_1\ \theta'_l)$. The coefficients $a$ and $\alpha_1$ are defined by Mellor (1977) and Bougeault (1981a) as:

$$a = \left(1 + \frac{L}{R_v T_l}\frac{L}{c_p T_l} q_{sl}\right)^{-1}, \qquad \alpha_1 = q_{sl}\left(\frac{L}{R_v T_l^2}\right)\frac{T}{\theta}, \tag{1.12}$$

where $T_l = T/\theta\ \theta_l$ and $q_{sl} = q_s(T_l)$. For a normalized variable $\zeta = s/\sigma_s$ having a probability density function $G(\zeta)$ where

$$\sigma_s = \frac{a}{2}\ (\overline{q'^2_w} + \alpha_1^2\overline{\theta'^2_l} - 2\alpha_1\overline{\theta'_l q'_w}\ )^{1/2}, \tag{1.13}$$

the partial cloudiness $N$, and the grid averaged liquid water content $q_l$ are given by:

$$N = \int_{-Q_1}^{+\infty} G(\zeta)d\zeta \tag{1.14}$$

$$q_l/2\sigma_s = \int_{-Q_1}^{+\infty} (Q_1 + \zeta)\ G(\zeta)d\zeta, \tag{1.15}$$

where $Q_1 = a(q_w - q_{sl})/2\sigma_s$.

In a higher-order turbulence model, the second-order moments involved in (1.13) are predicted and the only problem is to specify the probability density function $G(\zeta)$. In the present low-order turbulence model, $\overline{q'^2_w}$, $\overline{\theta'^2_l}$ and $\overline{\theta'_l q'_w}$ have to be parameterized. Several approaches have been proposed in the past. Smith (1990) expressed $\sigma_s$ as a function of an arbitrary critical relative humidity, while Tjernström et al. (1988) suggested a prognostic equation for $\sigma_s$. In order to make use of the original expression for $\sigma_s$ , we simply estimate the unknown second-order moments with the K-closure framework (a justification of this approach is given in B92a):

$$\overline{a'b'} = 2\frac{c_K}{c_{ab}}\ l_K\ l_\epsilon \frac{\partial a}{\partial z}\frac{\partial b}{\partial z}, \tag{1.16}$$

where $a$ and $b$ are either of the variables $\theta_l$ or $q_w$. The set of three constants $c_{ab}$ in (1.16) requires further discussion. From a large collection of convective boundary layer data,

Isaka and Guillemet (1983) reported that $c_{\theta\theta} = 2.6$ and $c_{qq} = 1.8$. As for $c_{\theta q}$, the fitted value was about 1.2 for Sc clouds. However, the dissipation closures used in higher order turbulence modeling retain only one single value for the three coefficients $c_{ab}$. This value was equal to 1.3 in Bougeault (1981b) when modeling the trade-wind cumulus, while in the Sc regime a value of 2.5 is generally adopted (Moeng and Randall, 1984; Bougeault, 1985). Here we use $c_{ab} = 2.5$ so that $\sigma_s$ is written as:

$$\sigma_s = \frac{a}{2}(c_1\ l_K\ l_\epsilon)^{1/2}\left[\left(\frac{\partial q_w}{\partial z}\right)^2 + \alpha_1^2\left(\frac{\partial \theta_l}{\partial z}\right)^2 - 2\alpha_1\frac{\partial q_w}{\partial z}\frac{\partial \theta_l}{\partial z}\right]^{1/2}, \qquad (1.17)$$

where $c_1 = 2c_K c_{ab}^{-1}$ is a numerical constant of value 0.32. Note that an equivalent derivation of (1.16) was also obtained by Redelsperger and Sommeria (1986), but they included a rather complex stability correction which has been ignored here. A more complete discussion of the parameterization of the second order moments used in (1.16) and (1.17) is given in section 1.3.

In order to close the condensation scheme we still have to prescribe the probability density function $G(\zeta)$. At present time no satisfactory formulation is available. Several distribution laws ranging from simple triangular functions (Smith 1990) to more elaborate functions (Bougeault 1981a; 1982) with a zero (Gauss), positive (truncated Exponential) or adjustable skewness factor (Gamma) have been proposed. Although the latter formulation introduced by Bougeault (1982) gives the best results when $N$ is less than a few percent, it is inapplicable for our scheme since the skewness factor (with accepted values between -2 and 2) must be given *a priori*. We therefore identified $G(\zeta)$ as a Gauss function for which the integrals in (1.14) and (1.15) are analytically tractable. This choice is further supported by the computations made by Bougeault (1981a) which showed that the skewness factor is close to zero at both cloud base and cloud top. Finally, with $G(\zeta) = \frac{1}{\sqrt{2\pi}} e^{-\zeta^2/2}$ we get:

$$N = \frac{1}{2}\left(1 + erf\frac{Q_1}{\sqrt{2}}\right) \qquad (1.18)$$

$$q_l/2\sigma_s = N\ Q_1 + e^{\frac{-Q_1^2/2}{\sqrt{2\pi}}}, \qquad (1.19)$$

where $erf$ is the error function.

*c) RADIATION CALCULATIONS*

Accurate radiative computations are performed using the ECMWF radiation scheme based on earlier works made by Fouquart and Bonnel (1980), and Morcrette et al. (1986). The only departure from the original ECMWF scheme (Morcrette 1989) is that the effective radius, $r_e$ is calculated by

$$r_e = \left(\frac{3\rho q_c}{4\pi\rho_l n_c}\right)^{(1/3)} \exp(\sigma_c^2), \qquad (1.20)$$

where it is assumed that the cloud droplets have a log-normal distribution with variance parameter $\sigma_c = 0.2775$ and total number concentration $n_c$. Here, $n_c$ is supposed constant in space and time with a value of 50 $cm^{-3}$, a typical value for maritime clouds. The

radiation code includes a special treatment of partial cloud cover (surface fraction) which, strictly speaking, should not be confused with the partial cloudiness (volume fraction) as calculated by the model. We therefore assume that these two quantities are identical, an assumption which is justified by the high vertical model resolution.

*d) NUMERICAL ASPECTS*

An accurate representation of radiative exchanges and turbulent entrainment at cloud top and at cloud base necessitates a high vertical resolution. We assume that the chosen uniform vertical grid with a grid spacing of 50 m is a reasonable compromise between numerical accuracy and computational cost. The model time step is set to 20 s while the numerically expensive calculations of radiation and turbulent length scales are made every 360 s and 60 s, respectively. Furthermore, the turbulent length scales are time averaged for numerical stability purposes.

### 1.2. Testing the model against reference cases

This section is devoted to test a 1D version of the model against numerical and observational data. The model has been tested against reference cases where the turbulence inside the CTBL was either driven by bouyancy effects (Nicholls and Leighton 1986), by wind shear effects, or by the common action of both effects (Brost et al. 1982a,b). A description of these tests is given in B92a. Here we focus on the observation of a stratiform cloud sheet over United Kingdom coastal water, where the turbulence is driven by buoyancy fluxes generated by longwave radiative cooling. We use the data to study the diurnal cycle of the marine CTBL in the midlatitudes.

*a) A BUOYANCY DRIVEN CTBL*

Following Turton and Nicholls (1987) and Duynkerke (1989), hereafter referred to as D89, we use aircraft observations made on 16 November 1983 off the north west of Scotland as reported by Nicholls and Leighton (1986). As in D89 the simulation is made for 1 July in order to test the diurnal variation of the CTBL under summertime radiation conditions, when solar absorption in the cloud deck is strong enough to induce a stable zone with cumulus clouds appearing just near the condensation level. A similar case has already been studied by Bougeault (1985) with the third-order turbulence closure model COLT. The results obtained with the present model SALSA are subjected to a comparison with the results of the COLT model, using a dissipation length formulation similar to (1.11b).

TABLE 1.1 Characteristics of the buoyancy case.

| | |
|---|---|
| Date | 1 July 1983 |
| Initial time (LST) | 0000 |
| Simulation time (h) | 48 |
| Latitude (°N) | 57 |
| Sea surface temperature (K) | 284.5 |
| Surface pressure (hPa) | 1020 |
| Divergence ($s^{-1}$) | $3\times10^{-6}$ |
| Initial bound. layer height (m) | 1150 |

The simulation parameters are given in Table 1.1. A large scale divergence is applied

in order to limit the rise of the boundary layer top. The air directly above sea level is assumed to be saturated. The initial wind is constant with height and equal to the geostrophic wind ($u_g = 0$ and $v_g = -7$ m s$^{-1}$). The initial profiles for the liquid potential temperature and the total water content are given by the dashed lines in Fig. 1.1. The boundary layer is initially well mixed and capped by a strong inversion ( $\Delta\theta_l = 10$ K, and $\Delta q_w = -3.5$ g kg$^{-1}$). The 48 hour evolution of the cloud liquid water content is illustrated in Fig. 1.2, where a Gaussian function has been used in the partial cloudiness scheme. The initially solid cloud deck undergoes important diurnal variations. Its thickness varies from 600 m in the early morning hours to 200 m at 1400 LST. During the daytime we actually distinguish a secondary cloud layer with very low liquid water content. This layer appears more clearly if we look at the evolution of the partial cloudiness visualized in Fig. 1.3. The cloudiness scheme simulates partial cloudiness at cloud top and at cloud base. We observe a completely saturated solid Sc cloud deck and a secondary cloud layer with cloudiness of about 10 - 20 % . These values indicate that cumulus clouds are present, a result which has already been noticed by Turton and Nicholls (1987).

The rising of the condensation level during the day and the partial evaporation of the Sc cloud deck is initiated by radiative heating in the lower part of the cloud. However, the strong radiative cooling at cloud top is nearly balanced by entrainment and subsidence. The influence of the radiative warming on the dissipation of the cloud deck is twofold: on the one hand it forms the stable zone near cloud base and so leads to the decoupling (the cloud is cut off from the surface heat and moisture fluxes as indicated in Fig. 1.1 by the noon profiles for $\theta_l$ and $q_w$), and on the other hand it directly promotes the evaporation of the cloud. This suggests that a solid cloud deck may be partially dissipated during daytime. In the afternoon the radiative heating gradually decreases. Consequently, the cloud deck reforms and reconnects to the subcloud layer during nighttime conditions as it appears in Figs. 1.2. and 1.3.

The turbulent structure of the buoyancy is represented in Fig. 1.4 by the TKE budgets at 1600 LST and at 0400 LST (28 hours of simulation) simulated by SALSA and COLT. The two models reproduce the same boundary layer structure, wind shear effects are negligible. As we expect, the turbulent structure of the CTBL undergoes a strong diurnal cycle. At daytime (Figs. 1.4a and 1.4b), the cloud layer characterized by positive buoyancy is decoupled from the subcloud layer. The decoupling is indicated by the zero values of buoyancy in the stably stratified zone at cloud base. At night (Figs. 1.4c and 1.4d), the buoyancy is positive throughout the CTBL and the cloud is much thicker than during daytime. The comparison shows that the structure as well as the magnitude of the TKE budget terms computed by the two models are in good agreement for both the decoupled (Figs. 1.4a and 1.4b) and well-mixed (Fig. 1.4c and 1.4d) boundary layer. In fact, the main difference between the two simulations can be found in the cloud thickness. The model COLT produces a somewhat thicker cloud layer than that predicted by for the four displayed regimes.

If we compare our results to the results of D89, who used a similar $K - \epsilon$ model but without partial cloudiness scheme, we see that the evolution of the cloud layer is close to that simulated by D89 (see Fig. 7 in D89). However, noticeable differences are found in the buoyancy maxima which are much weaker in D89 than those computed by SALSA and COLT (see Figs. 9 and 10 in D89). This may be due to the different formulation of the

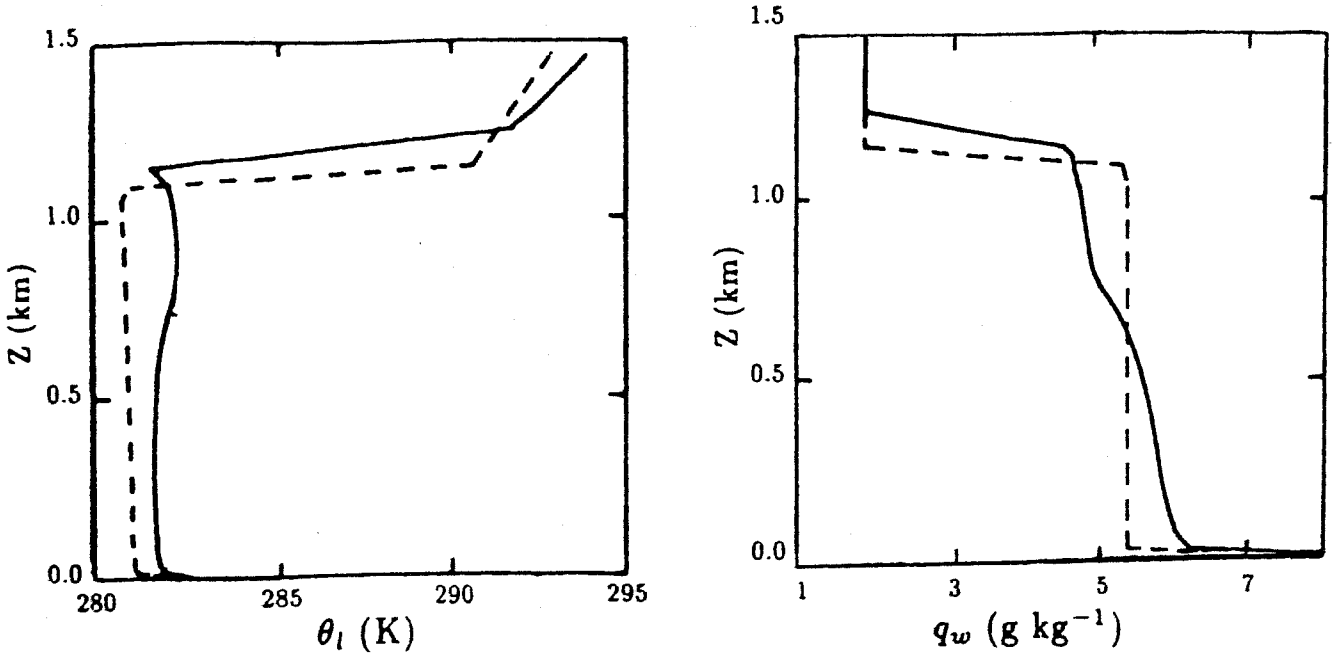


Fig. 1.1 Profiles of the liquid potential temperature and the total water content. Dashed lines: initial profiles, solid lines: profiles at 1200 LST.

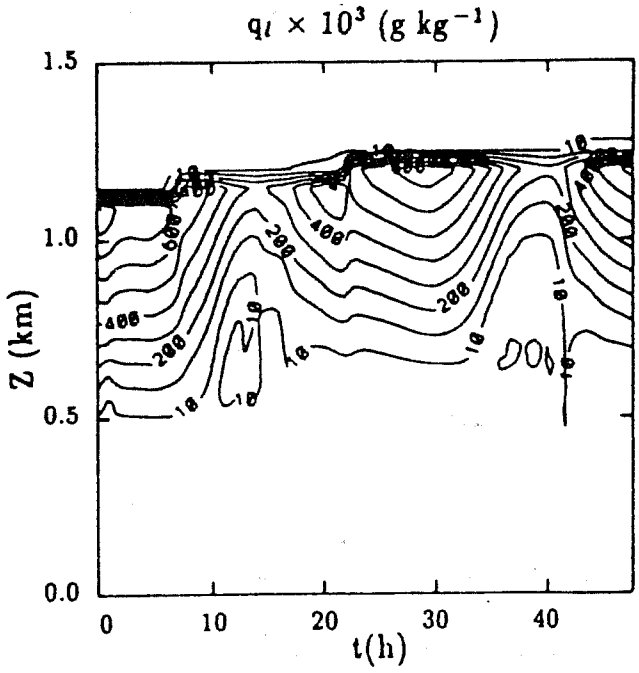


Fig. 1.2. 48 hours time-height section of the liquid water content.

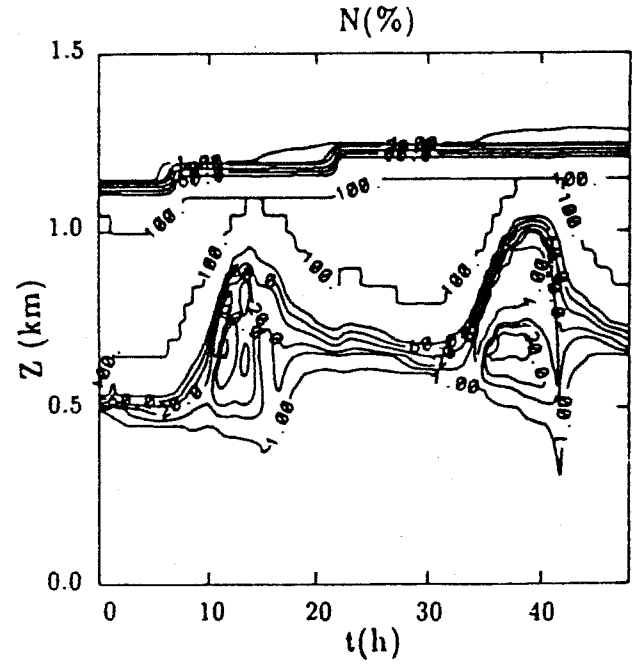


Fig. 1.3. 48 hours time-height section of the partial cloudiness obtained with a Gauss function.

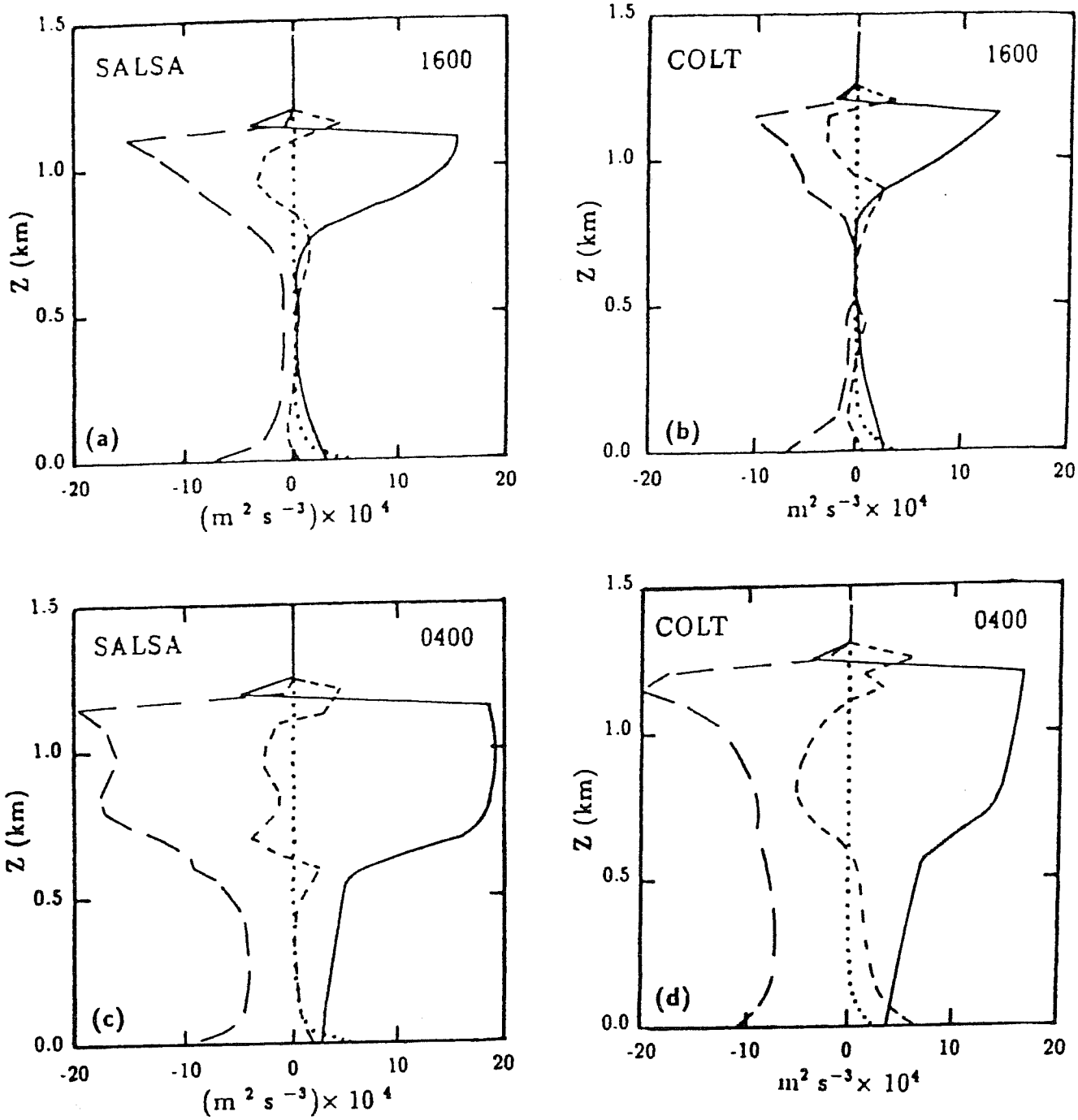


Fig. 1.4. Comparison of the turbulent kinetic energy budgets computed by the models SALSA and COLT at 1600 (a) and 0400 LST (b). Solid lines: buoyancy, long-dashed lines: dissipation, dotted lines: shear production, short-dashed lines: turbulent transport.

mixing and dissipation lengths used in SALSA and in D89.

*b) CLOUDINESS TRANSITION STUDY*

In this section we apply the partial cloudiness scheme to data from a cloudiness transition case observed off the California coast during FIRE and reported by Betts and Boers (1990), hereafter referred to as BB90. The cloudiness transition between the clear sky region and the region with a solid Sc cloud deck extended over a zone of roughly 50 km. A detailed description of the experiment and the large scale atmospheric conditions is given in the cited reference. The authors presented soundings for each of the different cloudiness regions, i.e. for the clear sky region, the region with cumulus clouds as well as for the regions with a broken and solid Sc cloud deck. This dataset is therefore particularly appropriate for 1D simulations. We apply our model to each of the four soundings which are denoted following BB90 by "clear", "cumulus", "broken" and "stratocumulus". Our main interest is to know whether the partial cloudiness scheme is able to reproduce the four different cloudiness regimes.

TABLE 1.2. Characteristics of the cloudiness transition study.

| | |
|---|---|
| Date | 7 July 1987 |
| Initial time (LST) | 1000 |
| Simulation time (h) | 4 |
| Latitude (°N) | 31.6 |
| Divergence ($s^{-1}$) | $5\times10^{-6}$ |

| | clear | cumulus | broken | stratocumulus |
|---|---|---|---|---|
| Sea surface temperature (K) | 290.1 | 290.1 | 289.7 | 288.9 |
| Sea surface pressure (hPa) | 1018.8 | 1017.9 | 1017.3 | 1016.4 |
| Initial bound. layer height (m) | 400 | 400 | 580 | 670 |

The simulations are done for four hours where the model solution is assumed to be stationary. Table 1.2 gives the simulation parameters for the four simulated cloudiness regimes. The imposed divergence of $5\times10^{-6}$ $s^{-1}$ corresponds to a typical climatological value. We see that the clear sky region, which actually is situated closer to the large scale pressure system, is characterized by a surface pressure which is about 2.4 hPa higher than in the Sc region. Furthermore, the sea surface temperature also increases by 1.2 K from the Sc to the clear sky region. The initial (dashed lines) and final profiles (solid lines) of $\theta_l, q_w$ and the horizontal wind components u and v are displayed in Figs. 1.5-1.7 The profiles are shown at the end of the simulation. As in the previous studies, the initial wind is taken equal to the geostrophic wind. The $\theta_l$ profiles (Fig. 1.5) show the existence of a well-mixed subcloud layer for each cloudiness regime, the atmosphere above the boundary layer is stable. A thin unstable layer just beneath boundary layer top can be observed in the $\theta_l$ profile for the broken cloud regime (Fig. 1.5c) and more clearly for the Sc regime. This unstable layer results from cloud top radiative cooling. When we start at the clear sky region and pass to the Sc region we observe a rise in boundary layer height of about 300 m . Consequently, the condensation level, which is situated near z=400 m, is attained

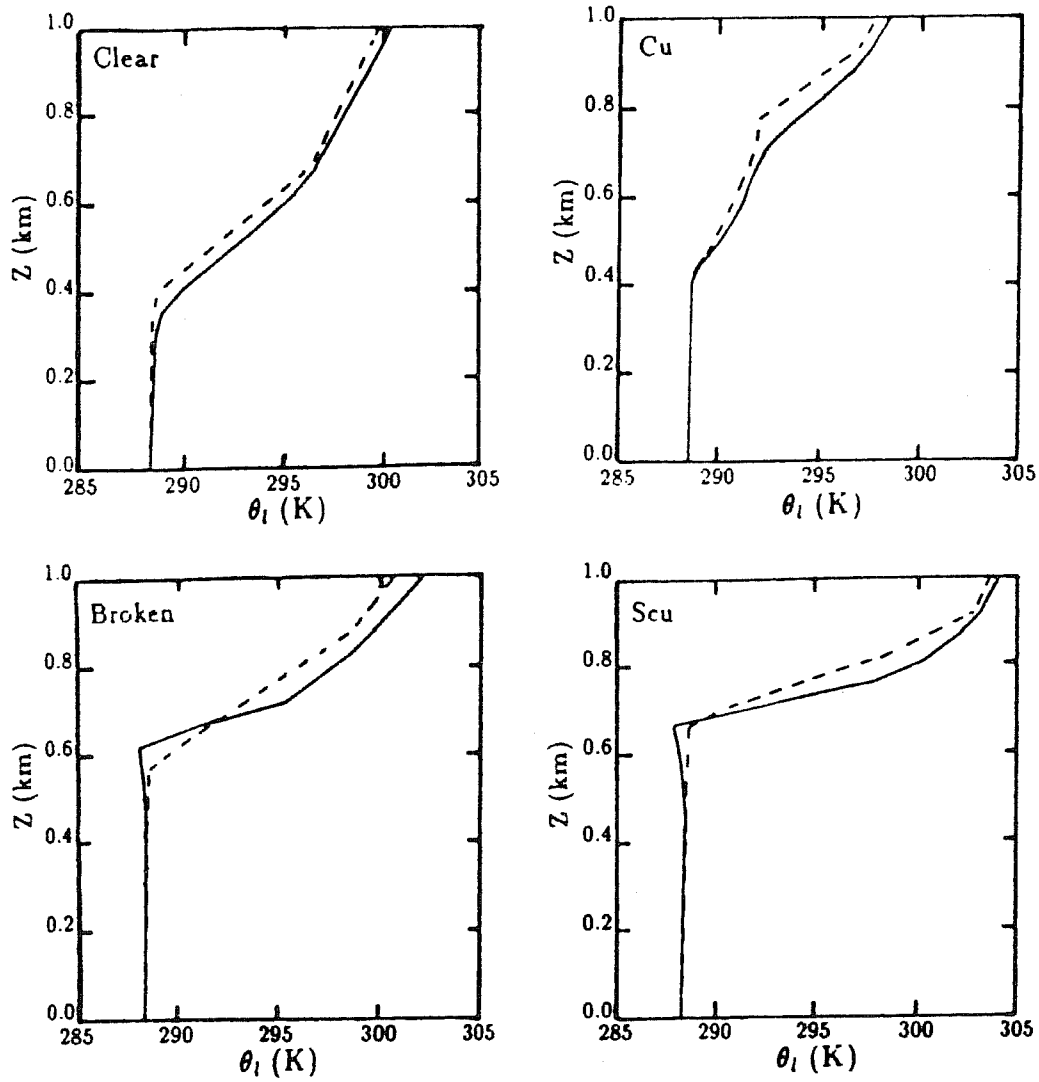


Fig. 1.5. Initial (dashed lines) and final profiles (solid lines) of the liquid potential temperature for the clear sky (a), cumulus (b), broken cloud (c) and solid Sc cloud regime.

in the Sc region with a boundary layer height of 680 m, whereas the boundary layer top in the clear sky region is lower than the condensation level. Furthermore, the temperature jump at boundary layer top strengthens with increasing cloudiness. The increase of the temperature jump at boundary layer top with increasing cloudiness qualitatively agrees with the cloud top entrainment instability criterion given by Randall (1980). Similar features as for the $\theta_l$ profiles can be found in the $q_w$ profiles (Fig. 1.6). However, Figs. 1.6a,b show rather complicated profiles characterized by a dry layer at z=700 m and a moist layer above. BB90 noted that horizontal advection in the upper part of the boundary layer is responsible for the particular humidity profiles in the clear sky and cumulus region. The wind profiles are displayed in Fig. 1.7. The horizontal wind for the broken cloud and Sc cloud regimes is rather strong with u=7 m $s^{-1}$ and v=-9 m $s^{-1}$, and there is practically no vertical wind shear (Figs. 1.7c,d). The wind shear becomes important at boundary layer top for the cumulus and clear sky regimes (Figs. 1.7a,b). Sensitivity studies (not reported) confirmed that the existence of a wind shear at boundary layer top can effectively reduce the cloud water content.

The vertical profiles of the partial cloudiness and the liquid water content are shown in Fig. 1.8. The model produces a totally covered sky for the Sc regime and partial cloudiness of 90 % and 40 % for the broken cloud and cumulus regime respectively (Fig. 1.8a). The value of 40% cloudiness for the cumulus regime is higher than the value reported by BB90. Sensitivity experiments (not shown) done with variable large scale divergence showed that the cloudiness varied by about 50% with respect to the given value when the divergence is doubled or halfed. In light of these experiments and the fact that the large scale divergence is a horizontally varying parameter the value of 40% cloudiness for the cumulus regime still appears reasonable, but seems slightly exagerated.

The maximum liquid water content varies from 0.35 g $kg^{-1}$ for the Sc to 0.17 g $kg^{-1}$ for the broken cloud region and to 0.03 g $kg^{-1}$ for the cumulus covered region (Fig. 1.8b). Note that these values are grid volume averaged values. The liquid water content of the cloudy part of the grid volume is given by $q_l/N$, so that the mean maximum in-cloud liquid water content for the the cumulus clouds is about 0.08 g $kg^{-1}$ and 0.2 g $kg^{-1}$ for the broken cloud structures. Adding the value of 0.35 g $kg^{-1}$ for the Sc clouds, we retrieve a typical linear increase of the liquid water content with cloud thickness.

In the following we will use the preceeding case studies in order to answer three important questions for cloud modeling: i) What is the precision of the partial cloudiness scheme (i.e. what is the precision of the parameterization of the second-order moments)? ii) Can the use of a partial cloudiness scheme assure a better model stability by avoiding an abrupt onset of condensation ?, and iii) what's about the vertical resolution required to represent clouds with a partial cloudiness scheme that depends on the vertical resolution only.

### 1.3 Partial Cloudiness and Modeling

*a) CALIBRATION OF THE SECOND-ORDER MOMENTS*

The crucial point of the partial condensation scheme is the parameterization of the second-order thermodynamic moments by the gradients of the mean prognostic variables, multiplied by a length scale factor and by the constant $c_1$. In order to test this parameterization, the three moments $\overline{\theta_l'^2}$, $\overline{q_w'^2}$ and $\overline{\theta_l' q_w'}$ as diagnosed in SALSA by (1.16) are compared to those

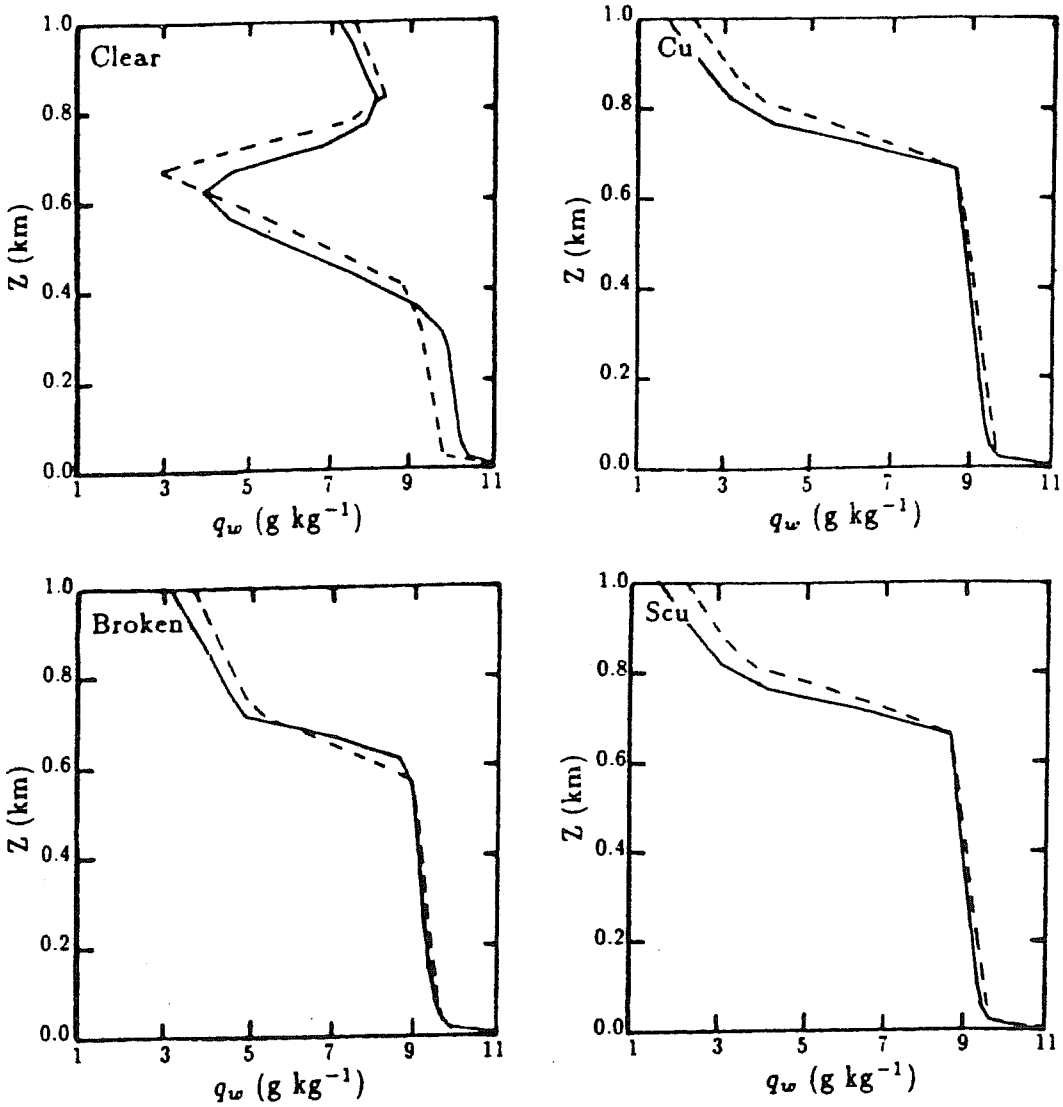


Fig. 1.6. As in Fig. 1.5 but for the total water content.

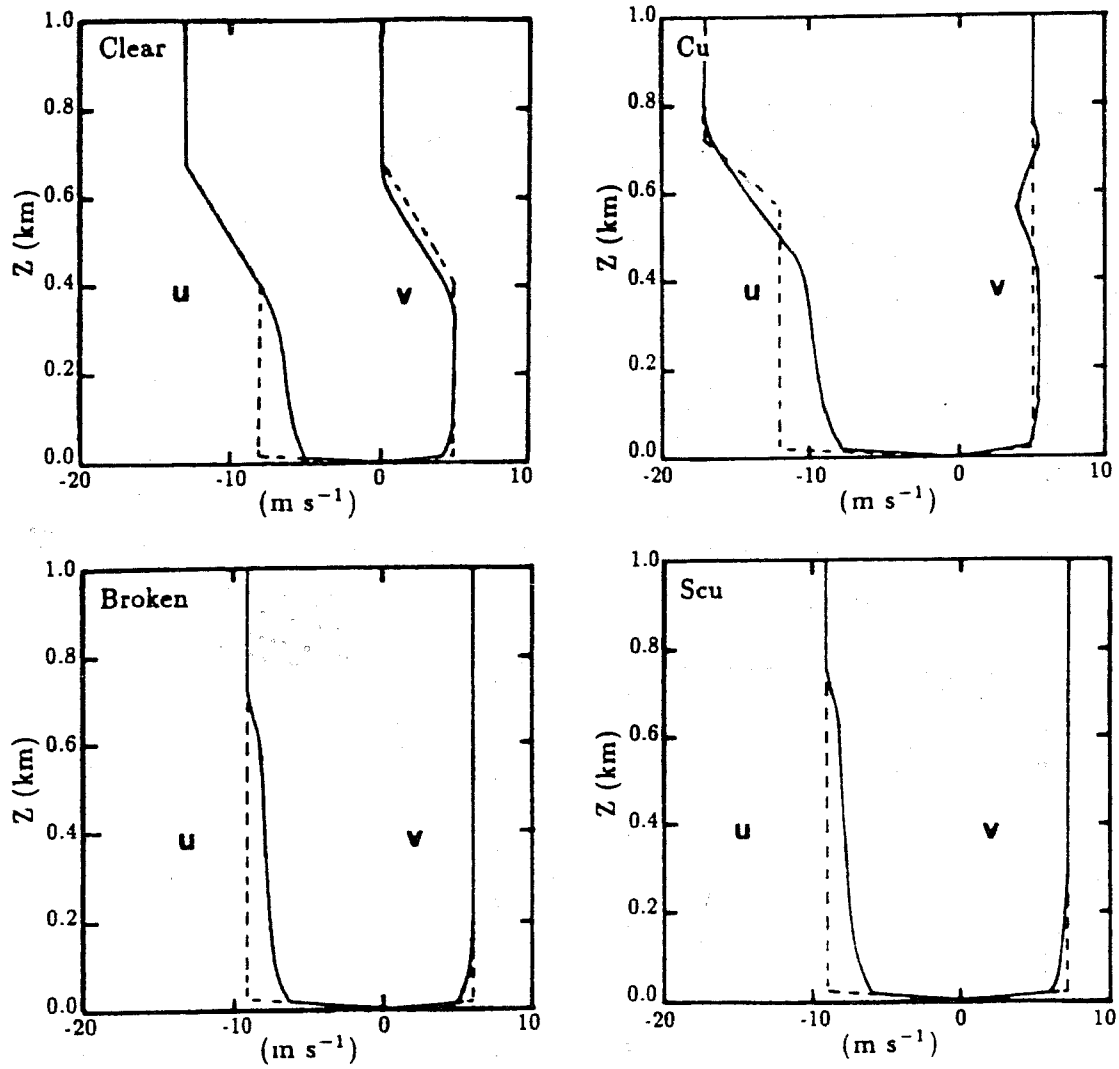


Fig. 1.7. As in Fig. 1.6 but for the horizontal wind components $u$ and $v$.

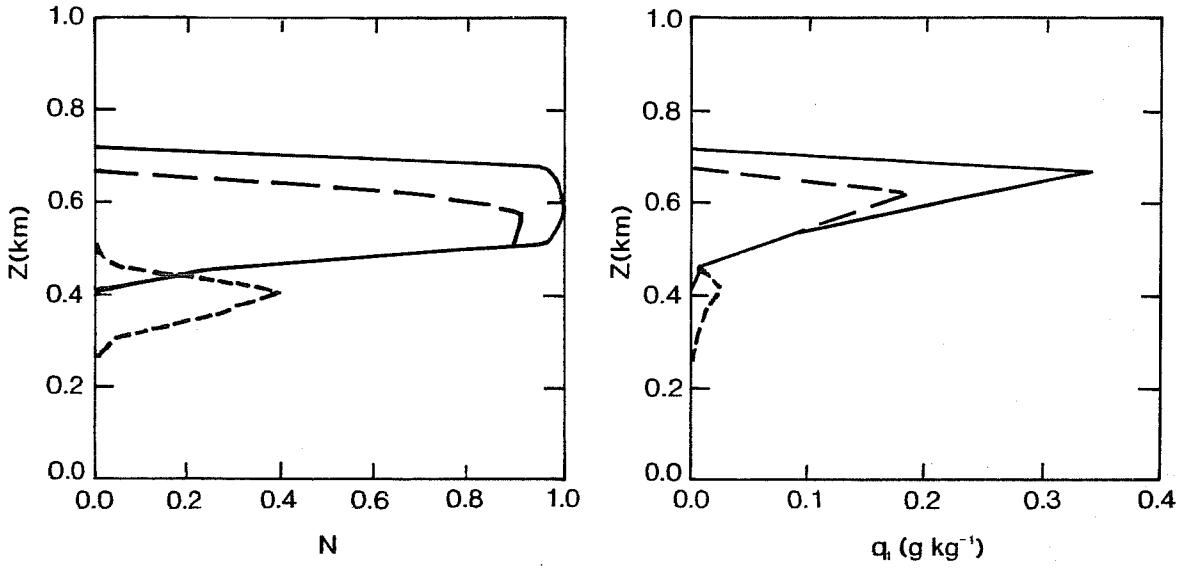


Fig. 1.8 Vertical profile of the partial cloudiness (a) and the liquid water content (b) for the different cloudiness regimes. Solid line: stratocumulus, long dashed line: broken cloud, short dashed line: cumulus.

generated by the prognostic equations of the third-order model COLT. This comparison is realized with the aid of two stationary solutions obtained with the initial data set used in the case of a purely buoyancy driven CTBL (section 1.2). The two stationary solutions correspond to solar radiation conditions fixed at 0000LST and 1200 LST, respectively. The vertical profiles of the three moments are depicted in Fig. 1.9a for a well-mixed nocturnal boundary layer, while Fig. 1.9b represents a decoupled cloud layer during the day. The maximum discrepancy between the results of SALSA (solid lines) and COLT (dashed lines) occurs for $\overline{q_w'^2}$ in Fig. 1.9a. However, the comparison shows that both the vertical structure as well as the maximum values are reasonably well reproduced by (1.16), with the maximum peak values during the night. Furthermore, because the partial condensation scheme is primarily concerned by the standard deviation $\sigma_s$, defined in (1.13), we have reported the profiles of $\sigma_s$ in Fig. 1.10. For the nighttime solution (Fig. 1.10a), the $\sigma_s$ profiles are nearly identical and the discrepancy is smaller than 20% during the decoupling at local noon. We also note that the double maximum in the $\sigma_s$ profile in Fig. 1.10b is well parameterized by (1.16). The present comparison shows that the neglection of the turbulent transport term in the derivation of (1.16) constitutes a reasonable simplification.

We now investigate the sensitivity of the partial cloudiness computations to the choice of the constant $c_1$. The parameterization given by (1.16) is only of general interest when the calculations of the partial cloudiness, $N$, are not critical to the choice of $c_1$. The sensitivity study can be done analytically because $N$ given by (1.18) is a function of $Q_1$ only, and $Q_1$ is directly proportional to $c_1^{-1/2}$. We calculate $N$ as a function of the product $Q_1 c_1^{1/2}$, which is independent of $c_1$, for three different values of $c_1$: 0.16, 0.32 and 0.48. Fig. 1.11 shows the graphs corresponding to different values of $c_1$. $N$ is a point symmetrical function with respect to $(Q_1 = 0; N = 0.5)$ because a gaussian probability density function has been used to obtain (1.18). The graphs shown are therefore nearly identical for values of $Q_1 c_1^{1/2}$ between -0.3 and 0.3, i.e. when $N$ varies between 0.3 and 0.7 . The relative error becomes large for low values of $N$, but the most important fact is that the absolute error made in $N$ does not exceed 0.1, even when $c_1$ is varied by a factor of three from 0.16 to 0.48 . This is a very appeasing result. A statistical partial cloudiness scheme used for meso- or large scale applications cannot be expected to produce values of $N$ which are correct to, say 0.1. Additional errors produced in the model by an inadequate choice of the constant $c_1$ are of the same order of magnitude. We recall that the partial condensation scheme is designed to better represent cloudiness transitions (vertically and horizontally) and therefore this scheme contains a reasonable compromise between numerical efficiency and sufficient physical realism.

*b) PARTIAL CLOUDINESS AND MODEL STABILITY*

In order to show the influence of the use of a partial cloudiness scheme on the model stability we have redone the simulation of the cumulus case using now an "all or nothing" (AON) condensation scheme. We recall that a value of $Q_1 = 0$, i.e. the water vapor content has just attained its saturation value, corresponds to partial cloudiness of 50 % (Fig. 1.11). Therefore, the AON scheme should simulate a completely saturated layer or a completely overcast sky for the broken cloud regime (partial cloudiness $\geq$ 50 %), and a clear sky for the cumulus regime (partial cloudiness $<$ 50 %) . We expect that the most striking differences between the partial condensation (PC) scheme and the AON scheme are obtained for the

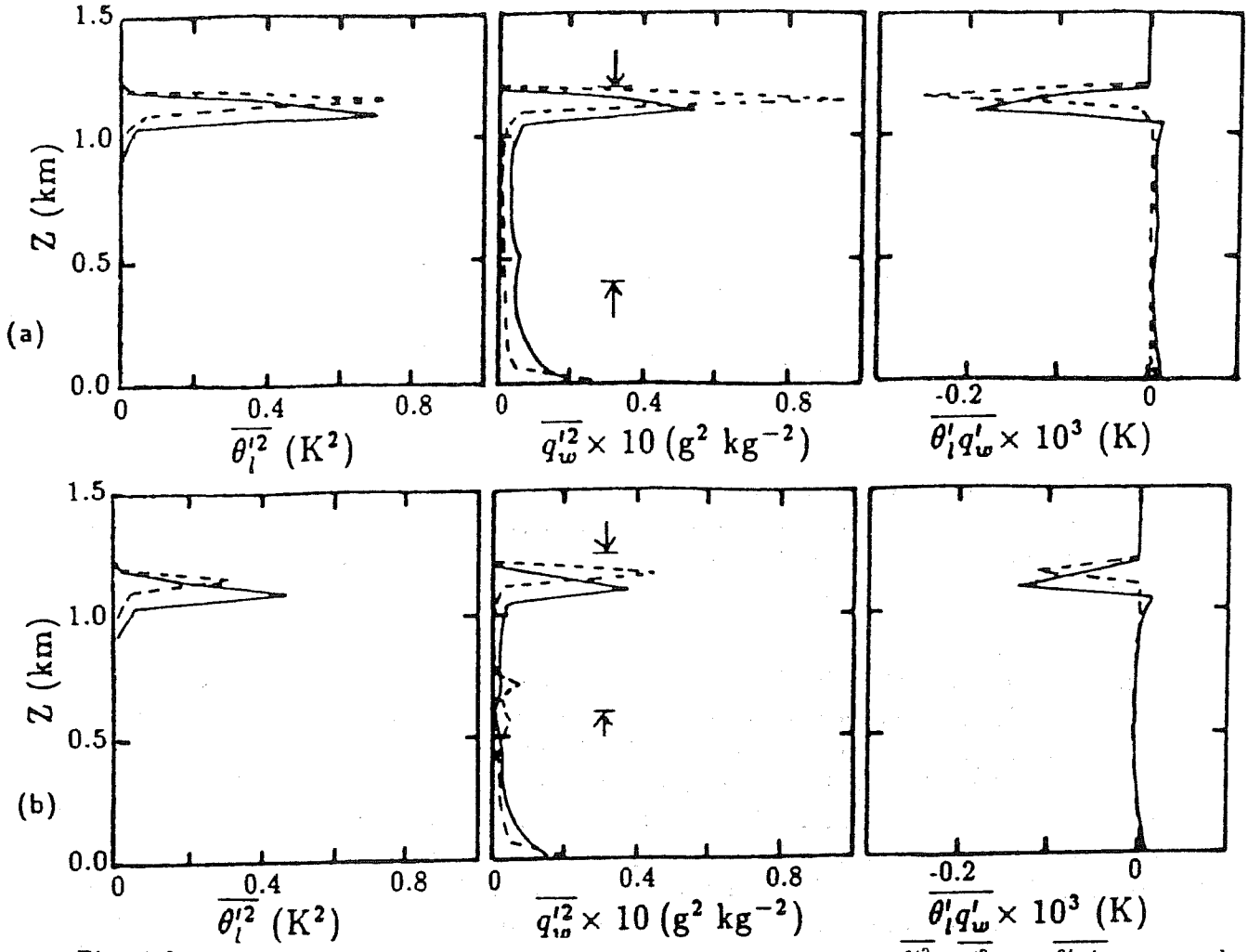


Fig. 1.9. Comparison of the thermodynamic second-order moments $\overline{\theta_l'^2}$, $\overline{q_w'^2}$ and $\overline{\theta_l' q_w'}$ computed by the models SALSA (solid lines) and COLT (dashed lines) with solar radiaton conditions fixed at 0000 LST (a) and 1200 LST (b). The cloud layer defined by $N > 1\%$ is located between the vertical arrows.

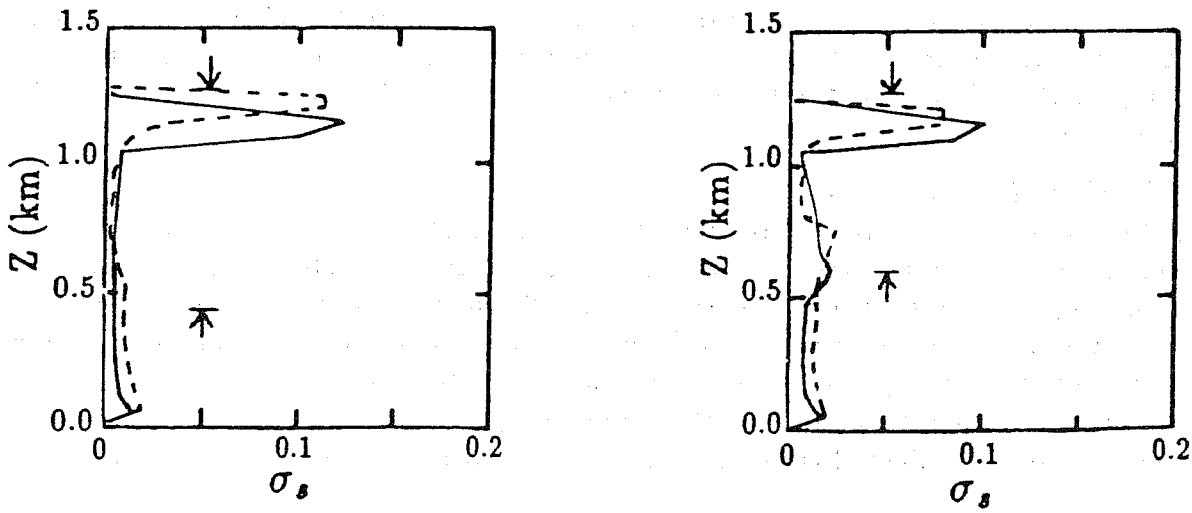


Fig. 1.10. As in Fig. 1.9 but for the standard deviation $\sigma_s$ defined in (15).

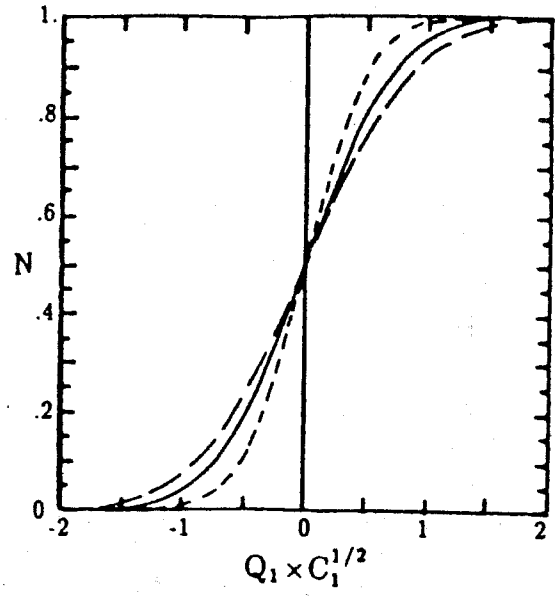


Fig. 1.11. Partial cloudiness $N$ computed with different values of the constant $c_1$. Short-dashed line: $c_1=0.16$, solid line: $c_1=0.32$, long-dashed line: $c_1=0.48$. The thick vertical line indicates the separation between zero and total cloudiness as computed by an "all or nothing" condensation scheme.

cumulus regime with partial cloudiness of 40 %, a value which is close to the critical value of 50 % . The difference between the two schemes becomes clear Fig. 1.12 where we plotted the evolution of the cloud water content. With the PC scheme (Fig. 1.12a), a quasi-stationary solution with maximum cloud water content of 0.03 g $kg^{-1}$ is obtained after 2 hours, whereas the AON scheme (Fig. 1.12b) produces spurious oscillations in the cloud water content, the final solution is a clear sky. Because the liquid water content simulated by the partial condensation scheme is very low (0.03 g $kg^{-1}$), the thermodynamic profiles obtained with the two schemes are rather similar. However, because the partial cloudiness intervenes directly in the buoyancy production term in (1.9c) the evolution of the TKE obtained with the two condensation schemes should therefore be significantly different. Near the condensation level, more TKE is produced by the PC scheme (Fig. 1.13a) due to the condensation processes. Furthermore, the model solution reaches a quasi-stationary state after about two hours. The spurious oscillations found in the cloud water content obtained with the AON scheme (Fig. 1.12b) can also be detected in the evolution of the TKE (Fig. 1.13b). The abrupt onset of condensation in the AON scheme destabilizes the model solution.

*c) VERTICAL RESOLUTION*

The influence of the vertical resolution on the model results is shown by simulating the Cumulus case with vertical resolutions of $\Delta z$ of 25, 50, 100, and 200 m. The results are shown on Fig. 1.14 after 4 hours of simulation. We only show the vertical cloudiness and cloud water profiles. As a general rule one can say that a precise simulation of these profiles reflects a good representation of the dynamics of the CTBL.

The discussion will be limited to the cloudiness profiles as the results for the cloud water profiles are equivalent. Fig. 1.14 clearly shows that the cloudiness tends to increase

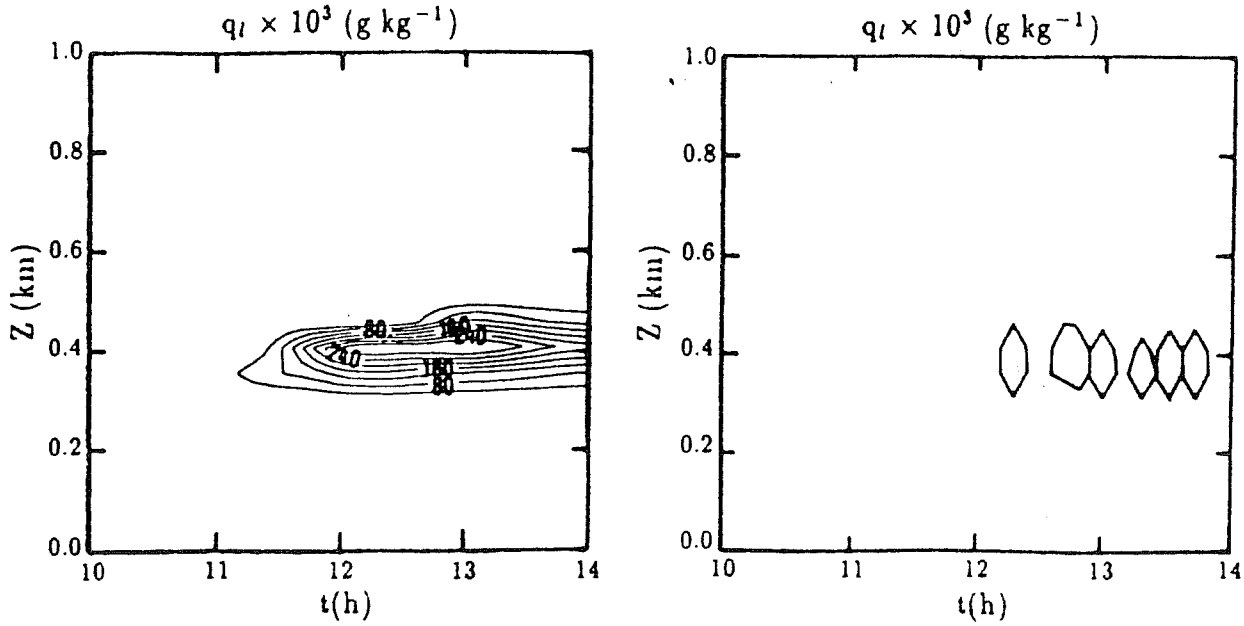


Fig. 1.12. 4 hours time-height section of the liquid water content obtained with a partial condensation scheme (a) and an "all or nothing" condensation scheme (b).

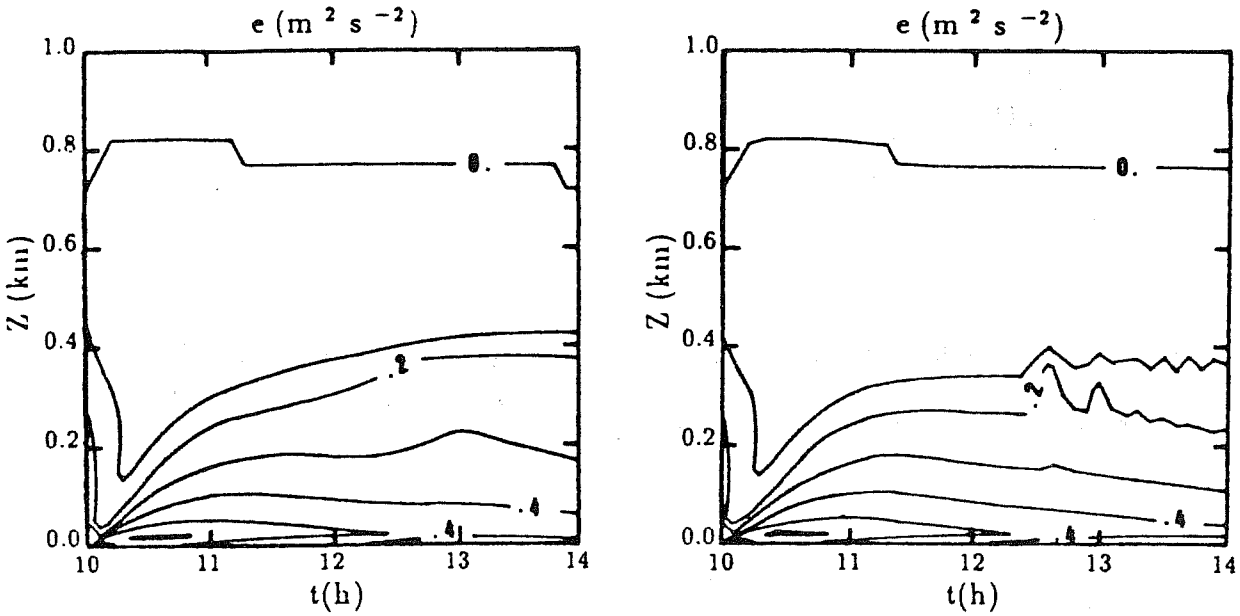


Fig. 1.13. As in Fig. 1.12 but for the turbulent kinetic energy.

with increasing $\Delta z$ (decreasing resolution). However, the profiles obtained with a resolution of 25 and 50 m are nearly identical. This is a very appeasing result, which shows that there exists a limit value for the necessary vertical resolution. We can conclude from Fig. 1.14 that a minimum number of model levels, say 3 or 4, is necessary to represent the dynamics of the cloud layer. This means for practical applications that a vertical resolution of 50 m is desirable. If this implies too much numerical burden a vertical resolution of 100 m might also be sufficient.

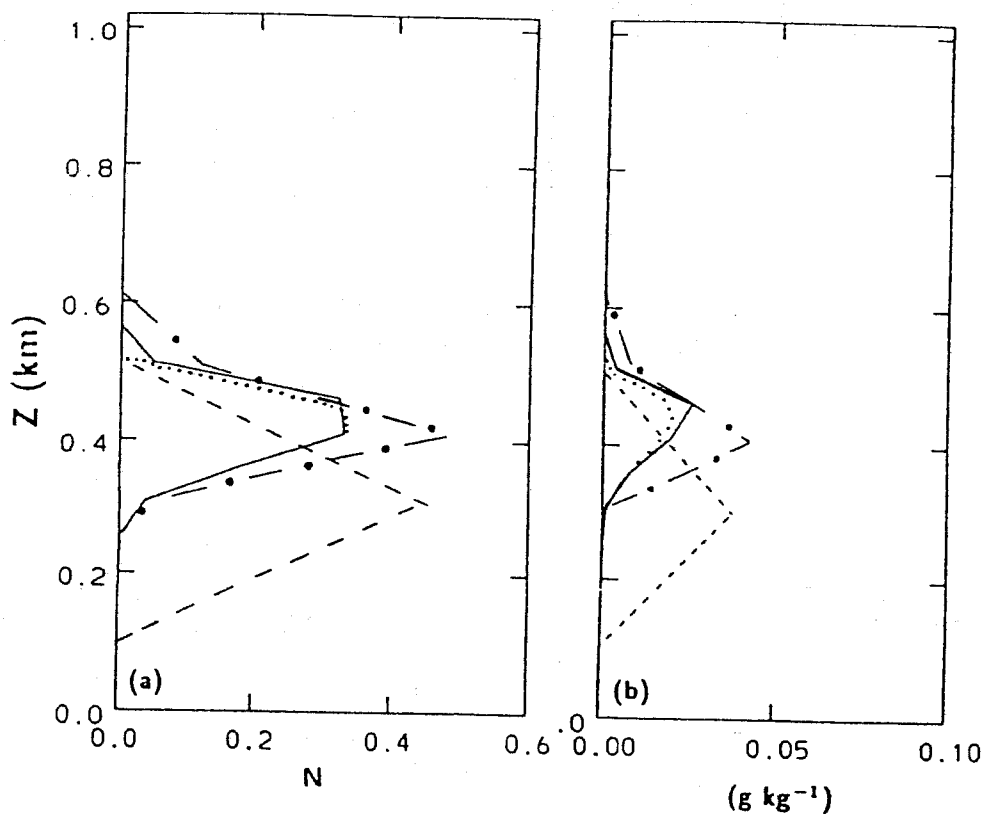


Fig. 1.14. Vertical profiles of the partial cloudiness (a) and the cloud water content (b) for different vertical model resolutions. Dotted lines: $\Delta z = 25$ m, solid lines: $\Delta z = 50$ m, dashed-dotted lines: $\Delta z = 100$ m, dashed lines: $\Delta z = 200$ m.

## On the use of partial cloudiness in a warm rain parameterization: A subgrid-scale precipitation scheme

### 2.1. Introduction

In recent mesoscale weather prediction models ( Sundqvist et al. 1989; Pudykiewicz et al. 1992; Ballard et al. 1991) and general circulation models (Smith 1990; Le Treut and Li 1991) precipitation, a sink for the cloud water content, is simply computed from an empirical formula describing the transformation of cloud water into rainwater. In these models, the effects of partial cloudiness on the precipitation rates have been introduced by utilizing the cloud-scale water content $q_c/N$, with $N$ the partial cloudiness, instead of the corresponding grid-scale value $q_c$. In the most recent model of Smith and Randall (1992), precipitation is calculated using a bulk microphysical parameterization, where the evaporation term is expressed as a function of the cloud-scale and environmental values of the temperature and the specific humidity, instead of using the corresponding grid-mean values. The cloud-scale and environmental variables are computed from the knowlege of the grid-scale partial cloudiness. However, only Chen and Cotton (1987) attempted to include in a more general way the effects of subgrid-scale variability in a rain parameterization by adding to the microphysical production terms of autoconversion and accretion the corresponding subgrid-scale correlation term.

We propose to handle the effects of partial cloudiness in a warm rain parameterization in a simple way, using only the parameter partial cloudiness. It will be shown that a realistic description of the microphysical processes of evaporation, autoconversion and accretion in partly cloudy layers must account for the vertical distribution of the partial cloudiness. Furthermore, the microphysical processes must be calculated using cloud-scale and environmental values of the thermodynamical variables instead of using their corresponding grid-mean values. Although these general ideas are valid for any microphysical scheme, they have been applied here to the Berry and Reinhardt warm rain parameterization (Berry and Reinhardt 1974). By predicting both the mixing ratios and number concentrations, the Berry and Reinhardt (BR) scheme is more general, and allows, as it was shown by Richard and Chaumerliac (1989), for a more accurate description of cloud microphysics than does the Kessler (Kessler 1969) parameterization. Indeed the developments presented in this paper can also be easily extended to the Kessler parameterization or to any other microphysical parameterization scheme.

### 2.2 Basic equations

As discussed in the first chapter thermodynamics are described by prognostic equations for the quasi-conservative variables liquid potential temperature $\theta_l$ and total water content $q_w$, defined by

$$\theta_l = \theta(1 - \frac{Lq_l}{C_pT}) \tag{1.1}$$

$$q_w = q_v + q_l; \quad \text{where} \quad q_l = q_c + q_r. \tag{2.2}$$

A list of symbols is provided in the Appendix. As a convention of notation all variables used denote grid averages at model level $k$. Only if necessary superscripts $k, k+1$ etc. will be

used. The cloud water content $q_c$ is diagnosed with the aid of a statistical partial cloudiness scheme using the saturation measure $\Delta = q_w - q_s(T_l) - q_r$ with $T_l = \theta_l(T/\theta)$, instead of $\Delta = q_w - q_s(T_l)$ in the original scheme (Mellor 1977), which does not consider precipitation. The cloud droplet concentration is a given model parameter, and is assumed constant in space and time. However, the rainwater content $q_r$ and its number concentration $n_r$ are calculated in the BR parameterization from prognostic equations. The complete set of conservation equations for the liquid potential temperature, the total water content, the rainwater mixing ratio and the total number concentration is:

$$\frac{d\theta_l}{dt} = -\frac{L\theta}{C_p T}\frac{\partial q_r}{\partial t}|_{\text{prec}} + \frac{\partial \theta_l}{\partial t}|_{\text{rad}} + F_{\theta_l} \tag{2.3a}$$

$$\frac{dq_w}{dt} = \frac{\partial q_r}{\partial t}|_{\text{prec}} + F_{q_w} \tag{2.3b}$$

$$\frac{dq_r}{dt} = \frac{\partial q_r}{\partial t}|_{\text{auto}} + \frac{\partial q_r}{\partial t}|_{\text{accr}} + \frac{\partial q_r}{\partial t}|_{\text{eva}} + \frac{\partial q_r}{\partial t}|_{\text{prec}} \tag{2.3c}$$

$$\frac{dn_r}{dt} = \frac{\partial n_r}{\partial t}|_{\text{auto}} + \frac{\partial n_r}{\partial t}|_{\text{self}} + \frac{\partial n_r}{\partial t}|_{\text{eva}} + \frac{\partial n_r}{\partial t}|_{\text{prec}}, \tag{2.3d}$$

where the operator $d/dt$ stands for the total derivative in an Eulerian coordinate system, and where $F$ denotes vertical turbulent diffusion. For simplicity, no vertical diffusion is applied to (2.3c) and (2.3d), as the turbulent fluxes of rainwater related (non-conservative) variables require a complex treatment (Redelsperger and Sommeria 1982). The radiation term has been retained in (2.3a). Store is laid here on the form of the microphysical production terms in (2.3c,d) as there are the terms for autoconversion, accretion, selfcollection, evaporation and precipitation. In the case of partly cloudy layers these terms apply only to the clear or cloudy parts of the numerical grid, in contrast to $q_r$ and $n_r$, which are average values over the cloudy and clear sky fraction of the grid.

## 2.3. Partial cloudiness in microphysics

Some of the production terms in (2.3c,d) can be calculated using the cloud-scale water content $q_c/N$, where $q_c$ and $N$ are the grid-mean cloud water mixing ratio and the partial cloudiness as obtained from the partial cloudiness scheme. Then, these terms are scaled (multiplied by $N$) in order to obtain grid-mean values of $q_r$ and $n_r$. However, some problems arise due to the fact that cloud water (cloudiness) and rainwater are independent variables. Therefore, when partly cloudy layers are present we do not know if raindrops are falling into the clear sky or cloudy fraction of the grid. This problem becomes apparent when we have to calculate the collection of cloud droplets by rain drops (accretion term) or the evaporation of rain in partly cloudy layers. In the following we will discuss the form of each production term in (2.3c,d) when a BR type parameterization is used together with a partial cloudiness scheme. All microphysical coefficients and constants appearing in the following discussion are explained in Berry and Reinhardt (1974), Nickerson et al. (1986) and Richard and Chaumerliac (1989).

*a. AUTOCONVERSION*

The conversion rate of cloud water into rainwater is given by:

$$\frac{\partial q_r}{\partial t}|_{\text{auto}} = \Psi_1 q_c^2 \tag{2.4a}$$

$$\frac{\partial n_r}{\partial t}|_{\text{auto}} = \Psi_2 \frac{\partial q_r}{\partial t}|_{\text{auto}}, \tag{2.4b}$$

where the $\Psi_x$ are constants or functions of parameters other than $q_c, q_r, n_c, n_r$. The effects of partial cloudiness $N$ can be simply taken into account by setting

$$\frac{\partial q_r}{\partial t}|_{\text{auto}} = \Psi_1 (q_c/N)^2 N = \Psi_1 q_c^2 F_{\text{auto}}; \quad F_{\text{auto}} = 1/N \tag{2.5a}$$

$$\frac{\partial n_r}{\partial t}|_{\text{auto}} = \Psi_2 \frac{\partial q_r}{\partial t}|_{\text{auto}}. \tag{2.5b}$$

The additional autoconversion factor $F_{\text{auto}}$ was obtained in (2.5a) by using the cloud-scale value $q_c/N$ and remultiplication by $N$. as autoconversion occurs in the cloudy part of the grid. Because equation (2.4a) is non-linear, different results are obtained when we calculate the autoconversion term using grid-mean values (2.4a) or when we calculate local production and then take the grid-mean (2.5a).

*b. ACCRETION*

The collection of cloud droplets by raindrops due to differences in the terminal velocity is given by:

$$\frac{\partial q_r}{\partial t}|_{\text{accr}} = \Psi_3 q_r q_c. \tag{2.6}$$

The problem of introducing the effects of partial cloudiness in (2.6) is more difficult than in (2.5) because we encounter a product of two independent variables, $q_r$ and $q_c$. While cloud water is concentrated in a fraction $N$ of the grid volume, rainwater can occur in both the cloudy and clear sky fraction of the grid volume. In order to determine the accretion rate in the presence of partly cloudy layers we have to estimate the grid fraction occupied by the rainwater, and to determine the horizontal overlap between the cloudy and rainwater fractions of the grid volume. In the present approach we only consider the two model layers $k$ and $k+1$ ($k$ is increasing with height).

Let us assume that the grid fraction occupied by $q_r^k$, the rainwater content in layer k can be estimated by the cloud cover between the top of the model and layer $k$ (for details see Bechtold et al., 1993). We now have to evaluate the portion of the rainwater which reacts with the cloud water. Three different vertical distributions of partial cloudiness (Fig. 2.1) have to be considered. In the first two scenarios the cloud fraction increases/decreases monotonically with height (Figs. 2.1a,b), whereas in the third scenario, the cloud layers separated by a clear sky layer overlap statistically. Three model layers with corresponding partial cloudiness $N^k, N^{k+1}$ and $N^{k+2}$ are depicted on each figure, and we wish to calculate the accretion rate in layer $k$ with the aid of an additional accretion factor in (2.6). The estimated raincover, $Cov_r$ is illustrated in Fig. 2.2 by the hatched areas together with the overlap region between $Cov_r$ and $N^k$ (shaded areas). The amount of rain from layer $k+1$

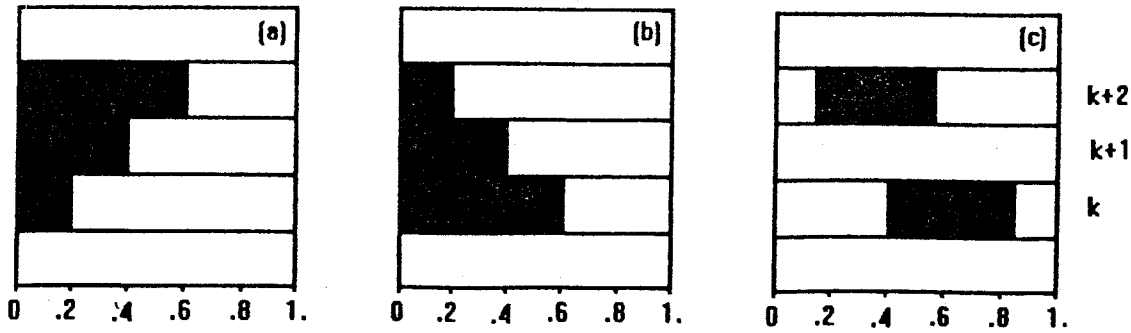


Fig. 2.1.Vertical distributions of the partial cloudiness: a). monotonically increasing with height, b). monotonically decreasing, c). statistical overlap.

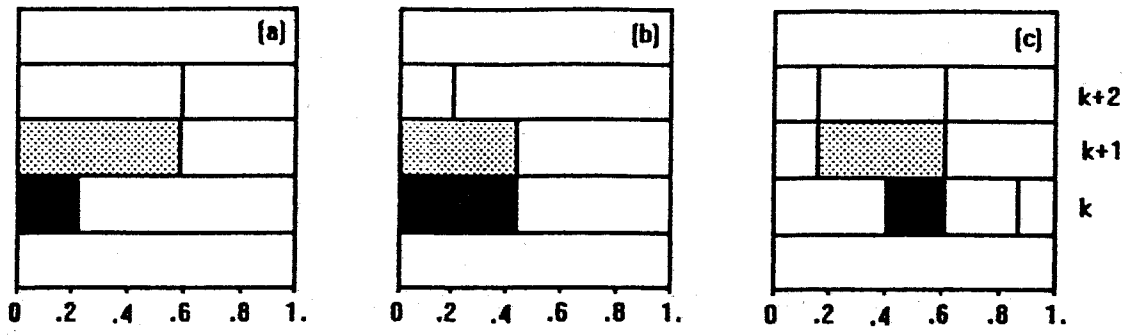


Fig. 2.2 Scheme corresponding to Fig.2.1, that allows to determine the amount of rainwater, covering the shaded fraction of layer $k+1$, that falls into the cloudy part of layer $k$. The overlap region is marked by the dark area.

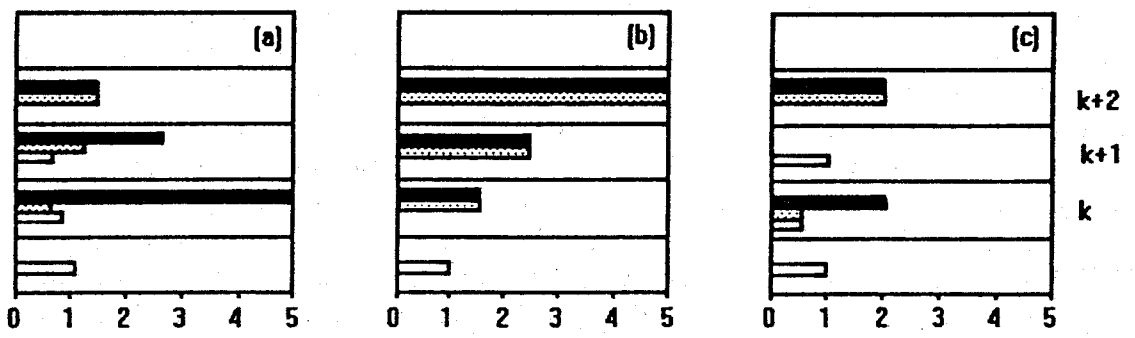


Fig. 2.3.Vertical distributions of the autoconversion factor (dark), the accretion factor (dash), and the evaporation factor (open), corresponding to the cloudiness profiles in Fig.1.

that can accrete cloud water in layer $k$ is proportional to the overlap between $Cov_r$ and $N^k$. Denoting these overlap areas by $\lambda$, and replacing $q_r$ and $q_c$ by their local values, we can easily derive the grid mean accretion rates for each scenario a). - c). of Fig. 2.2:

$$\frac{\lambda}{Cov_r}\frac{q_r}{Cov_r}\frac{q_c}{N}\ \lambda = q_r q_c \frac{N}{Cov_r^2}; \qquad \lambda = N \tag{2.7a}$$

$$\frac{q_r}{Cov_r}\frac{q_c}{N}\ \lambda = q_r q_c \frac{1}{N}; \qquad \lambda = Cov_r \tag{2.7b}$$

$$\frac{\lambda}{Cov_r}\frac{q_r}{Cov_r}\frac{q_c}{N}\ \lambda = q_r q_c N; \qquad \lambda = NCov_r. \tag{2.7c}$$

The leading factor $\lambda/Cov_r$ on the left-hand side of (2.7) gives the portion of the rainwater (scaled by its fractional cover) that can react with the cloud water; the final factor $\lambda$ is necessary in order to obtain grid-mean reaction (accretion) rates. In (2.7a) and (2.7b) $\lambda$ has been calculated from the maximum overlap assumption, whereas the random overlap assumption has been used in (2.7c). Note also that $q_r$ is the rainwater content at level $k$, and not at level $k+1$. The choice of $\lambda = Cov_r$ instead of $\lambda = N$ in (2.7b) assures the right expression in the limiting cases $Cov_r \to 0$ and $Cov_r = N$. We can now rewrite (2.6) with the accretion factors derived in (2.7):

$$\frac{\partial q_r}{\partial t}|_{\text{accr}} = \Psi_3 q_r q_c F_{\text{accr}} \tag{2.8}$$

$$q_r^{k+1} = 0 \qquad F_{\text{accr}} = 1/N$$

$$q_r^{k+1} > 0 \qquad F_{\text{accr}} = \begin{cases} N/Cov_r^2; & N^{k+1} > N^k \\ 1/N; & N^{k+1} \le N^k \\ N; & N^{k+1} = 0 \end{cases}$$

An interesting feature of (2.8) is that the so calculated accretion rate is lower ($F_{\text{accr}} < 1$) than in the original equation (2.6) if $q_r^{k+1} > 0$ and if $N < Cov_r^{1/2}$ or $N^{k+1}=0$. A result which is contradictory to that given in Chen and Cotton (1987), who proposed an unconditionally enhanced accretion rate due to subgrid scale correlations between $q_r$ and $q_c$. The difference is explained by the fact that (2.8) takes into account the possibility that rain falls into the clear sky fraction of the grid and so cannot interact with the cloud water.

As a last example we will derive the modified evaporation term, as the modified self-collection term can be derived similar to (2.8), and the precipitation term (by its definition as flux per unit surface) keeps unchanged.

*c) EVAPORATION*

The evaporation rate of rainwater is given by

$$\frac{\partial q_r}{\partial t}|_{\text{eva}} = \Psi_4 S(q_v - q_s(T))\ n_r, \tag{2.9}$$

where $S$ is the undersaturation.

In order to calculate the evaporation of rain in partly saturated layers we must know the temperature and the humidity in the clear sky fraction of the grid. To do so, we write the grid mean temperature and the grid mean specific humidity as a sum of their clear sky or unsaturated (superscript $u$) and cloudy or saturated (superscript $s$) fractions, respectively.

$$T = NT^s + (1-N)T^u \tag{2.10a}$$

$$q_v = Nq_v^s + (1-N)q_v^u \tag{2.10b}$$

$$q_v^s = q_s(T^s). \tag{2.10c}$$

This set of equations is not closed because we have three equations for four unknown variables. In order to close this system Xu and Randall (1992) assumed that the cloud-scale virtual temperature is equal to the environmental virtual temperature. However, when this closure is applied to (2.10), an iteration is necessary to compute $T^s$. Furthermore, the so computed cloud-scale temperature $T^s$ is not necessarily higher than the environmental temperature $T^u$. Instead, we propose to solve (2.10a) directly with the aid of the variable $T_l = \theta_l(T/\theta) = \theta_l(P/P_0)^{R/C_p}$ and the definition of $\theta_l = \theta(1 - Lq_c/C_pT)$. So that the solution of (2.10a) is

$$T^s = T_l + \frac{Lq_c/N}{C_p}; \quad T^u = T_l. \tag{2.11a}$$

This solution implies that the cloud-scale liquid potential temperature is approximately equal to the environmental liquid potential temperature, i.e. $\theta_l^s = \theta_l^u[1-O(10^{-4})]$. (2.11a) is consistent with the method by which the grid mean temperature $T = T_l + Lq_cC_p$ is computed in the model, and it ensures that $T^s > T > T^u$, which is verified in the absence of subsidence warming due to cumulus convection. Knowing $T^s$, $q_v^u$ is obtained from (2.10b)

$$q_v^u = \frac{q_v - Nq_s(T^s)}{1-N}. \tag{2.11b}$$

Equation (2.9) is linear with respect to the raindrop number concentration $n_r$. So we obtain the evaporation factor by dividing $n_r$ by its fractional coverage $Cov_r$, and by remultiplying (2.9) with the cloudless fraction of layer $k$ in which rainwater is present. This cloudless fraction is determined from Fig.2 and is $Cov_r - \lambda$, the difference between the raincover $Cov_r$ and the overlap region between $Cov_r$ and $N$. The evaporation factor then becomes $(Cov_r - N)/Cov_r = 1 - N/Cov_r$ for Fig. 2.2a, 0 for Fig. 2.2b, and $(Cov_r - Cov_rN)/Cov_r = 1 - N$ for Fig. 2.2c, so that the evaporation term writes:

$$\frac{\partial q_r}{\partial t}|_{\text{eva}} = \Psi_4 S(q_v^u - q_s(T^u))\ n_r\ F_{\text{eva}}, \tag{2.12}$$

$$F_{\text{eva}} = \begin{cases} 1 - N/Cov_r; & N^{k+1} > N^k \\ 0; & N^{k+1} \leq N^k \\ 1 - N; & N^{k+1} = 0. \end{cases}$$

Note that (2.12) differs from the original expression (2.9) not only by an additional factor $F_{eva}$ but also by the definition of the undersaturation which is now a function of $(q_v^u - q_s(T^u))$, instead of $(q_v - q_s(T))$ in (2.9).

*d. SUMMARY OF THE SCHEME*

The modified set of equations distinguishes from the original one by the use of additional factors taking into account the vertical distribution of the partial cloudiness, and by the use of incloud and environmental values for $T$ and $q_v$ in order to describe correctly the evaporation in partly cloudy layers. Whereas an additional autoconversion factor has already been considered by Redelsperger and Sommeria (1986), Chen and Cotton (1987), and Sundqvist et al. (1989), the authors did not consider the effects of partial cloudiness on the rain evaporation rate.

The work of the modified set of equations is illustrated in Fig. 2.3 where we have drawn the values of the additional microphysical factors $F_{auto}$ (shaded bars), $F_{accr}$ (hatched bars) and $F_{eva}$ (open bars) for the three cloudiness distributions shown in Fig. 2.1. Whereas the autoconversion factor is simply inversely proportional to the partial cloudiness, the accretion factor (selfcollection factor) depends on the cloudiness distribution considered. It has been chosen equal to the autoconversion factor for the uppermost partly cloudy layer and for distribution b), however its value varies between 0 and $1/N$ for the other distributions chosen. Concerning the evaporation factor, we see that it is zero for the cloudiness distribution b), but also for the uppermost partly cloudy layer of the other distributions. This is clearly different to the original formulation which would simulate evaporation because the grid mean humidity in a partly cloudy (saturated) grid is lower than its saturation value. However, the evaporation factor is one, so identical to the original formulation, in the subcloud layer.

## 2.4. Numerical example

The full advantages of the modified set of equations, especially of the modified evaporation equation (2.12), which utilizes the temperature and humidity in the cloudless part of the grid, can only be documented for realistic cases of subgrid-scale cloudiness and precipitation. The cumulus case, discussed in section 1.4 has been chosen for the numerical test. However, when partial cloudiness is simulated with the aid of a statistical partial cloudiness scheme, the corresponding cloud water content is in general rather low. As a consequence, the simulated rainwater content, and especially the microphysical terms of accretion and selfcollection are rather small. Nevertheless, our principal interest in the following numerical test is to realistically demonstrate the differences in the evaporation rates calculated with the original BR rain parameterization and the modified scheme.

The one-dimensional test has been run for one hour with a vertical resolution of 50 m and a time step of 10 s, during which the microphysical equations (2.3c,d) are integrated with a Runge-Kutta scheme of order four. The cloud droplet number concentration is set to 50 $cm^{-3}$, a typical value for marine boundary layer clouds. Furthermore, the solar radiation conditions are fixed to 1200 LST. All initial thermodynamical and turbulent profiles are balanced, and issue from the corresponding simulation described in section 1.4.

*a). CUMULUS CASE*

The corresponding initial vertical profiles of the partial cloudiness and the cloud water

content are depicted in Fig. 2.4. The cloudiness profile is close to the schematic profile depicted in Fig. 2.1a. It shows a cloud layer of 300 m thickness and maximum partial cloudiness of 37%. The maximum cloud water content (not shown) is 0.025 g $kg^{-1}$. The simulated evolution over one hour of the partial cloudiness, the cloud water content and the rainwater content is shown in Fig. 2.5. The partial cloudiness (Fig. 2.5a) scarcely varies during the simulation. Its maximum value reduces from 37% initially to 35% after one hour of simulation. However, the evolution of the cloud and rain water content is very rapid. After about ten minutes the cloud and rainwater content becomes stationary (Figs. 2.5b,c). The cloud has lost about 50% of its initial water content by precipitation. The maximum rainwater content attains a value of $3\times10^{-6}$ g $kg^{-1}$; a rather small value which is a factor of $10^4$ smaller than the maximum cloud water content.

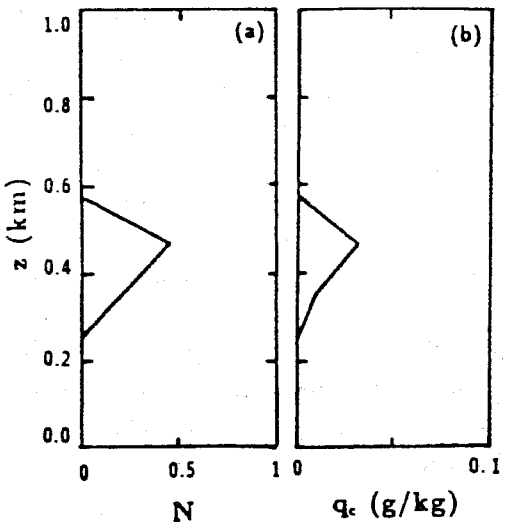


Fig. 2.4.Initial distributions of the partial cloudiness (a) and the cloud water content (b) for the cumulus case.

The additional microphysical factors of autoconversion ($F_{auto}$), accretion ($F_{accr}$) and evaporation ($F_{eva}$) used in the modified BR parameterization (Eqs. 2.5,8,12) are shown after 18 minutes of simulation in Fig. 2.6, where is also drawn the corresponding profile of the partial cloudiness. The profiles of the microphysical factors are close to those schematically depicted in Fig. 2.3a. However, the autoconversion factor shows a double maximum due to the low values of cloudiness at cloud top and cloud base. Note also that the accretion factor is greater than one in the layer with maximum cloudiness. The evaporation factor continuously increases from 0 to unity when one approaches the cloud base. The different evaporation rates calculated according to (2.9) with the original scheme (OS) and according to (2.12) with the modified scheme (MS) are illustrated in Fig. 2.7, where we have actually plotted the undersaturation multiplied by the evaporation factor (which is one in the OS). Fig. 2.7 shows remarkable differences between the two schemes. Whereas the MS does not allow for evaporation in the upper part of the cloud (the evaporation factor is zero), the OS simulates strong undersaturation and therefore evaporation. The differences between the two schemes persist in the lower part of the cloud, where the MS

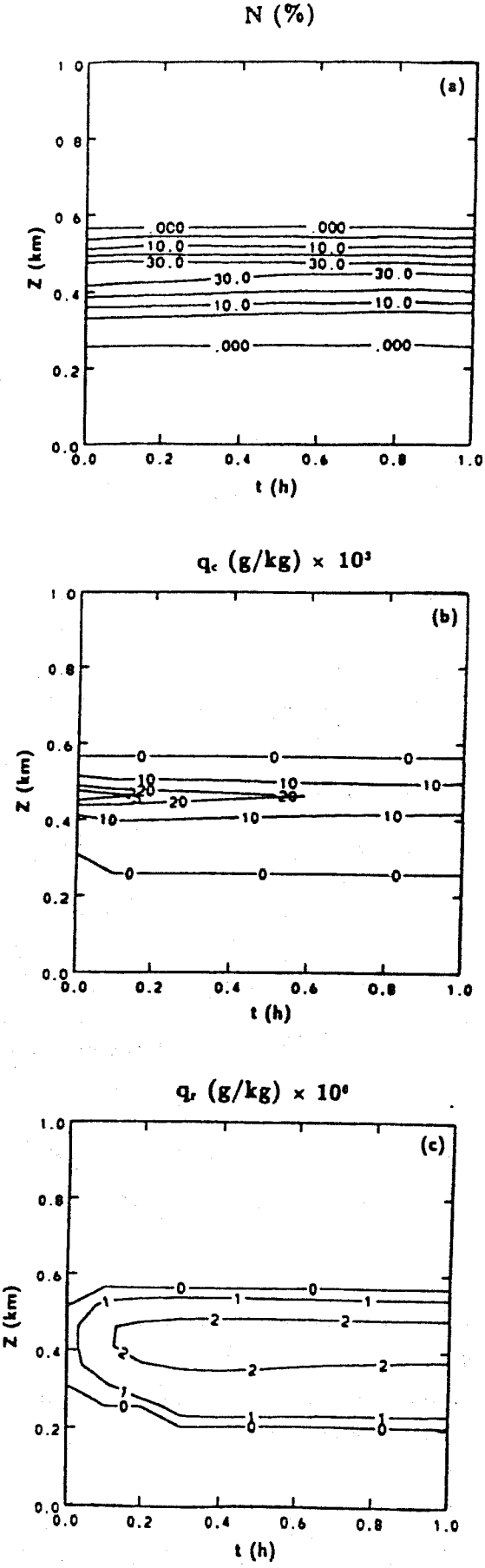


Fig. 2.5. 1 hour evolution of the partial cloudiness (a), the cloud water content (b), and the rainwater content (c).

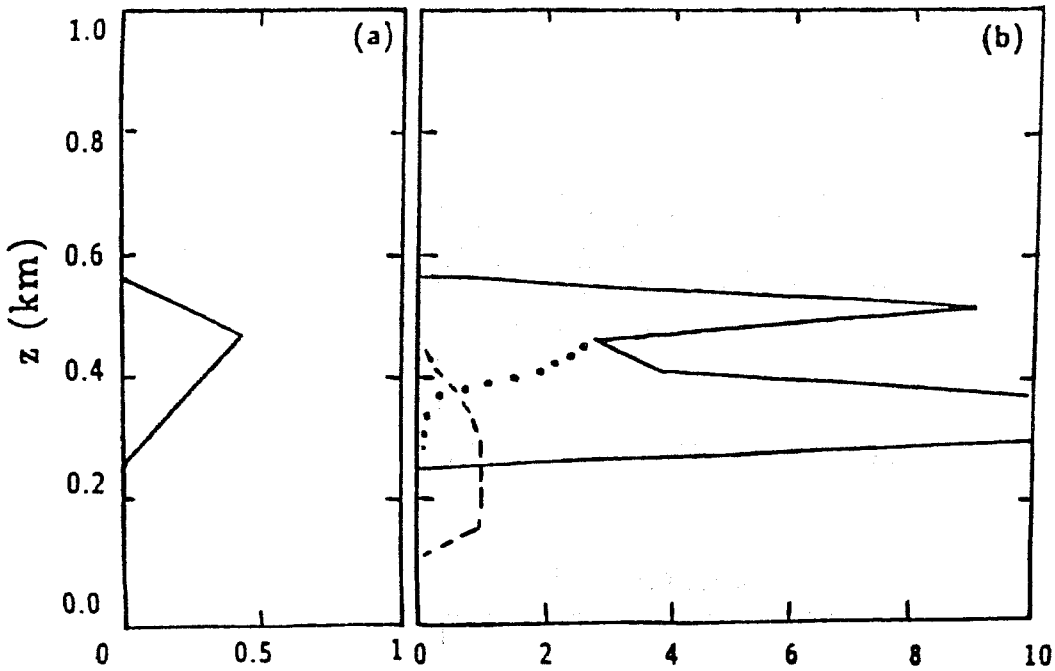


Fig. 2.6.Profile of the partial cloudiness after 1080 s, together with the corresponding profiles for the additional microphysical factors for autoconversion (solid line), accretion (dotted line), and evaporation (dashed line).

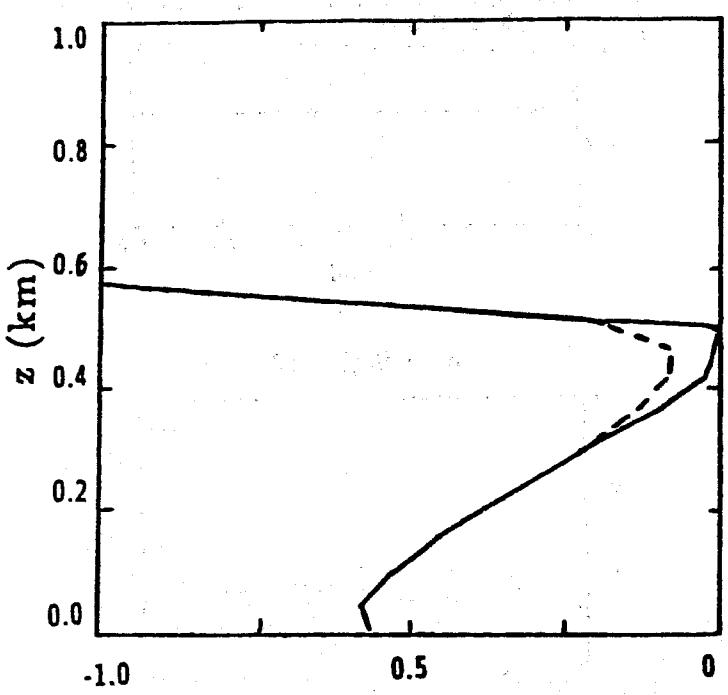


Fig. 2.7.Comparison of the vertical profiles of the saturation deficit multiplied by the evaporation factor, obtained with the modified scheme (solid line), and with the original scheme (dashed line).

smoothly approaches the OS when one approaches the cloud base. Finally, in Fig. 2.8 we compare the rainwater content obtained with the MS to that obtained with the OS. The results are shown after one hour of simulation. The MS produces a cloud water content which is about a factor of 6 larger than that obtained with the OS. Furthermore, in the MS scheme rain falls down to a height of 200 m, which is two levels below cloud base, whereas in the OS the rainwater content is so small that all rain immediately evaporates below cloud base. The differences in the rainwater content between the two schemes are mainly due to the higher autoconversion rate and lower evaporation rate simulated by the MS. About 70% of the difference in Fig. 2.8 can be explained by the additional autoconversion factor in the MS, but 30% of the difference is due to the different formulations of evaporation used in the two schemes.

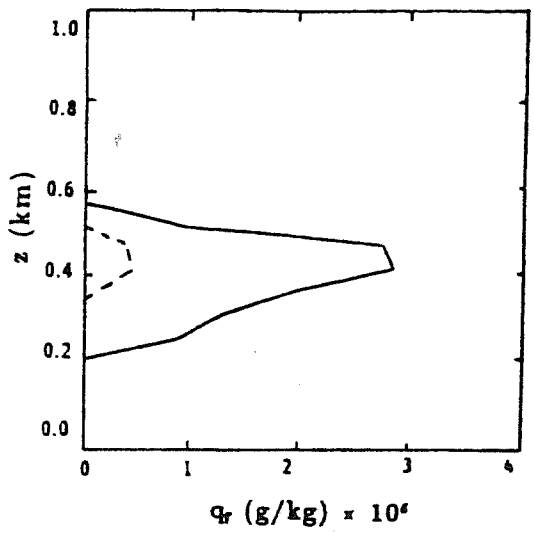


Fig. 2.8.Comparison of the vertical profiles of the rainwater content obtained with the modified scheme (solid line), and with the original scheme (dashed line).

**Summary and conclusions**

The interest of this seminar was to show that the CTBL including partial cloudiness can be reasonably well represented with a low-order turbulence model. The originality of the presented model is the manner in which the partial cloudiness scheme has been coupled with the turbulent scheme and the microphysical scheme. It has been shown that the partial cloudiness can be accurately and efficiently calculated with a diagnostic statistical partial cloudiness scheme, where the second-order thermodynamic moments are simply expressed as gradients of the mean variables multiplied by turbulent length scales.

The use of a partial cloudiness scheme efficiently avoids spurious oscillation in the liquid water content and the turbulent kinetic energy - as it might appear when a simple "all or nothing condensation scheme" is used - when the atmosphere is closed to its saturated state. The given formulation of the partial cloudiness is independent of the horizontal resolution of the model, however it requires a vertical resolution of typically 100 m.

Furthermore, a method has been proposed to include the effects of partial cloudiness in a microphysical scheme and to generate subgrid-scale precipitation. The proposed method essentially profits by two ideas: the use of the vertical profile of the partial cloudiness, and the use of cloud-scale and environmental values of the thermodynamic variables instead of their grid-mean values. As an example, these general ideas have been applied to a Berry and Reinhardt warm rain parameterization scheme.

The present model ensures a consistent computation of the physical processes in the cloud-topped boundary layer (turbulence, cloudiness, precipitation), and proposes a first step in developing methods for an explicit computation of precipitation amounts in partly cloudy regions. We think that the model presents a good compromise between physical realism and computational cost. The proposed parameterization of boundary layer cloudiness might be included in mesoscale and possibly even large scale models.

## APPENDIX

### List of principal symbols

| | |
|---|---|
| $c_1$ | numerical constant |
| $C_p$ | heat capacity |
| $Cov_r$ | grid fraction occupied by the rainwater |
| $f$ | Coriolis parameter |
| $e$ | turbulent kinetic energy |
| $K$ | mixing coefficient |
| $l_k, l_\epsilon$ | mixing/dissipation length |
| $L$ | latent heat of evaporation |
| $N$ | partial cloudiness |
| $n_c$ | cloud droplet concentration |
| $n_r$ | raindrop concentration |
| $P_0$ | reference pressure (1000 hPa) |
| $q_c$ | specific cloud water content |
| $q_l$ | specific liquid water content |
| $q_r$ | specific rainwater content |
| $q_s$ | saturation specific humidity |
| $q_v$ | specific humidity |
| $q_w$ | specific total water content |
| $r_e$ | effectiv radius |
| $R$ | gas constant for dry air |
| $t$ | time |
| $T$ | temperature |
| $u$ | wind component in the x direction |
| $u_g$ | geostrophic part of u |
| $v$ | wind component in the y direction |
| $v_g$ | geostrophic part of v |
| $w$ | vertical velocity |
| $z$ | vertical coordinate |
| $\alpha$ | autoconversion coefficient |
| $\theta$ | potential temperature |
| $\theta_l$ | liquid potential temperature |
| $\rho$ | density of air |
| $\rho_l$ | density of liquid water |
| $\sigma_0$ | dispersion parameter for the lognormal distribution |

## REFERENCES


Ballard, S. P., B. Golding and R. N. B. Smith, 1991: Mesoscale model experimental forecasts of the haar of northeast scotland. *Mon. Wea. Rev.*, **119**, 2107-2123.

Bechtold, P., C. Fravalo and J.-P. Pinty, 1992a: A model of marine boundary layer cloudiness for mesoscale applications. *J. Atmos. Sci.*, **49**, 1723-1744.

———, C. Fravalo and J.-P. Pinty, 1992b: A two-dimensional cloudiness study during a cold air outbreak event. *Bound. Layer Meteor.*, **60**, 243-270.

———, J.-P. Pinty and P. Mascart, 1993: The use of partial cloudiness in a warm rain parameterization: A subgrid-scale precipitation scheme. *Accepted for Mon. Wea. Rev.*

Berry, E. X., and R. L. Reinhardt, 1974: An analysis of cloud drop growth by collection: Part III. Accretion and self-collection. *J. Atmos. Sci.*, **31**,2118-2126.

Betts, A. K., and R. Boers, 1990: A cloudiness transition in a marine boundary layer. *J. Atmos. Sci.*, **47**, 1480-1496.

Bougeault, P., 1981a: Modeling the trade-wind cumulus boundary layer. Part I: Testing the ensemble cloud relations against numerical data. *J. Atmos. Sci.*, **38**, 2414-2428.

———, 1981b: Modeling the trade-wind cumulus boundary layer. Part II: A high-order one-dimensional model. *J. Atmos. Sci.*, **38**, 2419-2439.

———, 1982: Cloud-ensemble relations based on the gamma probability distribution for the higher-order models of the planetary boundary layer. *J. Atmos. Sci.*, **39**, 2691-2699.

———, 1985: The diurnal cycle of the marine stratocumulus layer: A higher-order model study. *J. Atmos. Sci.*, **42**, 2826-2843.

———, and J.-C. André, 1986: On the stability of the tird-order turbulence closure for the modeling of the stratocumulus-topped boundary layer. *J. Atmos. Sci.*, **43**, 1574-1581.

———, and P. Lacarrère, 1989: Parameterization of orography-induced turbulence in a mesobeta-scale model. *Mon. Wea. Rev.*, **117**, 1872-1890.

Brost, R. A., D. H. Lenschow and J. C. Wyngaard, 1982a: Marine stratocumulus layers. Part I: Mean conditions. *J. Atmos. Sci.*, **39**, 800-817.

———, J. C. Wyngaard, and D. H. Lenschow, 1982b: Marine stratocumulus layers. Part II: Turbulence budgets. *J. Atmos. Sci.*, **39**, 818-836.

Chen, C., and W. R. Cotton, 1987: The physics of the marine stratocumulus-capped mixed layer. *J. Atmos. Sci.*, **44**, 2951-2977.

Deardorff, J. W., 1976: On the entrainment rate of stratocumulus-capped mixed layer. *Quart. J. Roy. Meteor. Soc.*, **102**, 563-582.

———, 1980: Stratocumulus-capped mixed layers derived from a three-dimensional model. *Bound. Layer Meteor.*, **18**, 495-527.

Duynkerke, P. G., 1989: The diurnal variation of a marine stratocumulus layer: A model sensitivity study. *Mon. Wea. Rev.*, **117**, 1710-1725.

Fouquart, Y., et B. Bonnel, 1980: Computations of solar heating of the earth's atmosphere: A new parameterization. *Beitr. Phys. Atmosph.*, **53**, 35-62.

Isaka, H., and B. Guillemet, 1983: Molecular dissipation of turbulent fluctuations in the convective mixed layer. Part II: Height variations of characteristic time scales and experimental test of molecular dissipation models. *Bound. Layer Meteor.*, **27**, 257-279.

Kessler, E., 1969: *On the distribution and continuity of water substance in atmospheric circulations. Meteor. Monogr.*, **10**, No. 32, Amer. Meteor. Soc., 84 pp.

Le Treut, H., and Z.-X. Li, 1991: Sensitivity of an atmospheric general circulation model to prescribed SST changes: Feedback effects associated with the simulation of cloud optical properties. *Climate Dyn.*, **5**, 175-187.

Mellor, G. L., 1977: The gaussian cloud model relations. *J. Atmos. Sci.*, **34** , 356-358.

Moeng, C.-H., and D. A. Randall, 1984: Problems in simulating the stratocumulus-topped boundary layer with a third-order closure model. *J. Atmos. Sci.*, **41**, 1588-1600.

Morcrette, J.-J., 1989: Impact of changes to the radiation transfer parameterizations plus cloud optical properties in the ECMWF model. *Mon. Wea. Rev.*, **118**, 847-873.

————, L. Smith, and Y. Fouquart, 1986: Pressure and temperature dependances of the absorption in longwave radiation parameterizations. *Beitr. Phys. Atmos.*, **59**, 847-873.

Nicholls, S. and J. Leighton, 1986: An observational study of the structure of stratiform cloud sheets: Part I: Structure. *Quart. J. Roy. Meteor. Soc.*, **112**, 431-460.

Nickerson E.C., E. Richard, R. Rosset, and D. R. Smith, 1986: The numerical simulation of clouds, rain, and airflow over the Vosges and Black Forest mountains: A meso-$\beta$ model with parameterized microphysics. *Mon. Wea. Rev.*, **114**, 398-414.

Pudykiewicz, R., R. Benoît and J. Mailhot, 1992: Inclusion and verification of a predictive cloud-water scheme in a regional numerical weather prediction model. *Mon. Wea. Rev.*, **120**, 612-626.

Randall, D. A., 1980: Conditional instability of the first kind upside-down. *J. Atmos. Sci.*, **37**, 125-130.

Redelsperger, J. L., and G. Sommeria, 1982: Méthode de représentation de la turbulence associée aux précipitations dans un modèle tri-dimensionnel de convection nuageuse. *Bound. Layer Meteor.*, **24**, 231-252.

Redelsperger and G. Sommeria, 1986: Three-dimensional simulation of a convective storm: Sensitivity studies on subgrid parameterization and spatial resolution. *J. Atmos. Sci.*, **43**, 2619-2635.

Sommeria, G., and J. W. Deardorff, 1977: Subgrid-scale condensation in models of non-precipitating clouds. *J. Atmos. Sci.*, **34**, 216-241.

Richard, E., and N. Chaumerliac, 1989: Effects of different rain parameterizations on the simulation of mesoscale orographic precipitation. *J. Appl. Meteor.*, **28**, 1197-1212.

Smith, L. D., and D. A. Randall, 1992: Parameterization of cloud microphysics processes in the CSU General Circulation Model. *Atmospheric Science Paper No. 491*, Colorado State University.

Smith, R. N., 1990: A scheme for predicting layer clouds and their water content in a general circulation model. *Quart. J. Roy. Meteor. Soc.*, **116**, 435-460.

————, and J. W. Deardorff, 1977: Subgrid-scale condensation in models of nonprecipitating clouds. *J. Atmos. Sci.*, **34**, 344-355.

Sundqvist, H., E. Berge and J. E. Kristjánsson, 1989: Condensation and cloud parameterization studies with a mesoscale numerical weather prediction model. *Mon. Wea. Rev.*, **117** 1641-1657.

Tjernström, M., L. Enger and A. Andrén, 1988: A three-dimensional numerical model for studies of atmospheric flows on the meso-$\gamma$-scale. *J. Theoret. Appl. Mech.*, **7**, 167-194.

Turton, J. D., and S. Nicholls, 1987: A study of the diurnal variation of stratocumulus using a multiple mixed layer model. *Quart. J. Roy. Meteor. Soc.*, **113**, 969-1009.

Xu, K.-M., and D. A. Randall, 1992: The semi-empirical basis of a prognostic cloud parameterization for use in climate models. *Proceedings of the 11th International Conference of Clouds and Precipitation.* Montreal, Canada, 1992, pp. 1144-1147.